JOURNAL OF PETROLOGY | VOLUME 55 | NUMBER 4 | PAGES 709–747 | 2014 | doi:10.1093/petrology/egu004

Final Magma Storage Depth Modulation of Explosivity and Trachyte–Phonolite Genesis at an Intraplate Volcano: a Case Study from Ulleung Island, South Korea

MARCO BRENNA[1]*, RICHARD PRICE[2], SHANE J. CRONIN[1], IAN E. M. SMITH[3], YOUNG KWAN SOHN[4], GI BOM KIM[4] AND ROLAND MAAS[5]

[1]VOLCANIC RISK SOLUTIONS, MASSEY UNIVERSITY, PALMERSTON NORTH, NEW ZEALAND

[2]SCIENCE AND ENGINEERING, UNIVERSITY OF WAIKATO, HAMILTON, NEW ZEALAND

[3]SCHOOL OF ENVIRONMENT, UNIVERSITY OF AUCKLAND, AUCKLAND, NEW ZEALAND

[4]DEPARTMENT OF EARTH AND ENVIRONMENTAL SCIENCES, GYEONGSANG NATIONAL UNIVERSITY, JINJU, SOUTH KOREA

[5]SCHOOL OF EARTH SCIENCES, UNIVERSITY OF MELBOURNE, PARKVILLE, VIC 3010, AUSTRALIA

RECEIVED MAY 31, 2013; ACCEPTED JANUARY 14, 2014
ADVANCE ACCESS PUBLICATION FEBRUARY 13, 2014

Ulleung Island is the top of a 3000 m (from sea floor) intraplate alkalic volcanic edifice in the East Sea/Sea of Japan. The emergent 950 m consist of a basaltic lava and agglomerate succession (Stage 1, 1·37–0·97 Ma), intruded and overlain by a sequence of trachytic lavas and domes, which erupted in two episodes (Stage 2, 0·83–0·77 Ma; Stage 3, 0·73–0·24 Ma). The youngest eruptions, post 20 ka BP, were explosive, generating thick tephra sequences of phonolitic composition (Stage 4), which also entrained phaneritic, porphyritic and cumulate accidental lithics. Major element chemistry of the evolved products shows a continuous spectrum of trachyte to phonolite compositions, but these have discordant trace element trends and distinct isotopic characteristics, excluding a direct genetic relationship between the two end-members. Despite this, the Stage 3 trachytes and some porphyritic accidental lithics have chemical characteristics transitional between Stage 2 trachytes and Stage 4 phonolites. Within the phonolitic Stage 4 tephras three subgroups can be distinguished. The oldest, Tephra 5, is considerably enriched in incompatible elements and chondrite-normalized rare earth element (REE) patterns display negative Eu anomalies. The later tephras, Tephras 4–2, have compositions intermediate between the early units and the trachyte samples, and their REE patterns do not have significant Eu anomalies. The last erupted, Tephra 1, from a small intra-caldera structure, has a distinct tephriphonolite composition. Trace element and isotopic chemistry as well as textural characteristics suggest a genetic relationship between the phaneritic lithics and their host phonolitic pumices. The Stage 4 tephras are not related to earlier phases of basaltic to trachytic magmatism (Stages 1–3). They have distinct isotopic compositions and cannot be reliably modelled by fractional crystallization processes. The differences between the explosive phonolitic (Stage 4) and effusive trachytic (Stage 2–3) eruptions are mainly due to different pre-eruptive pressures and temperatures, causing closed- versus open-system degassing. Based on thermodynamic and thermobarometric modelling, the phonolites were derived from deeper (subcrustal) magma storage and rose quickly, with volatiles trapped until eruption. By contrast, the trachytes were stored at shallower crustal levels for longer periods, allowing open-system volatile exsolution and degassing before eruption.

KEY WORDS: *phonolite; trachyte; Ulleung; thermobarometry; explosive eruptions; effusive eruptions*

*Corresponding author. New address from 17 February 2014: Department of Geology, University of Otago, Dunedin, New Zealand. E-mail: brenna.marco@yahoo.co.nz.

INTRODUCTION

Evolved silicic rocks of alkalic affinity occur in many intraplate volcanoes and oceanic islands, often exhibiting a basaltic basement complex, topped by trachytic to phonolitic domes or calderas (Baker, 1969; Price & Taylor, 1973; Price *et al.*, 1985; Panter *et al.*, 1997; Ablay *et al.*, 1998; Kim *et al.*, 1999; Legendre *et al.*, 2005; Wiesmaier *et al.*, 2012). Because of the temporal and geochemical associations, the relationship between primitive and evolved lavas has generally been attributed to fractional crystallization processes (Coombs & Wilkinson, 1969; Nash *et al.*, 1969; Price & Chappell, 1975; Wörner & Schmincke, 1984; Price *et al.*, 1985; Le Roex *et al.*, 1990; LeMasurier *et al.*, 2003; Johansen *et al.*, 2005; White *et al.*, 2012), although crustal contamination and assimilation may also influence the line of descent (Panter *et al.*, 1997; Brenna *et al.*, 2012; Wiesmaier *et al.*, 2012). The occurrence of medium- to coarse-grained subvolcanic (hypabyssal) xenoliths in some of the eruption deposits has lent support to the fractionation theory (Kim *et al.*, 2008). However, there is commonly a gap in the spectrum of compositions between primitive and evolved rocks. Explanations for this 'Daly Gap' include crystal fractionation processes in a complex plumbing system (Dufek & Bachmann, 2010), magma mixing (Ferla & Meli, 2006) and crustal anatexis (Bailey, 1964; Hay & Wendlandt, 1995; Hay *et al.*, 1995; Price *et al.*, 2003; Legendre *et al.*, 2005). The nature of the processes controlling magmatic evolution in intraplate settings is thus still a topic of significant debate.

Phonolitic volcanism is not as common as other types of volcanism on Earth. Well-studied examples include Tenerife, Canary Islands (Johansen *et al.*, 2005), the Laacher See, Germany (Wörner *et al.*, 1983), Mount Erebus–Mount Morning–Marie Byrd Land volcanism, Antarctica (Panter *et al.*, 1997; Kelly *et al.*, 2008; Martin *et al.*, 2010), the Kenya rift (Price *et al.*, 1985) and Mount Vesuvius, Italy (Signorelli *et al.*, 1999). Lesser investigated phonolite volcanoes occur elsewhere; for example, Hoodoo Mountain, Canada (Edwards *et al.*, 2002), Monte Vulture, Italy (De Fino *et al.*, 1986), or the now extinct Dunedin volcano, New Zealand (Price *et al.*, 2003). Ulleung Island is as yet the only reported case of phonolitic volcanism in east Asia. Other large intraplate volcanoes in the region, such as Jeju Island, South Korea (Brenna *et al.*, 2012) or Changbaishan, China–North Korea (Wei *et al.*, 2007), tend to be trachytic or rhyolitic. Considered in this context, the study of Ulleung provides a fresh perspective on this type of volcanism both regionally and globally.

Understanding trachytic and phonolitic eruptions is of great importance in many parts of the world where the flanks of phonolitic intraplate alkalic volcanoes may be densely populated (e.g. Ulleung >10 000, Tenerife ~1 million, Vesuvius ~3 million) with seasonal tourism generally swelling the numbers. The way in which pre-eruptive storage conditions influence trachytic and phonolitic eruption mechanisms is not as yet well constrained, mainly because magmatic-gas driven explosive eruptions are rare, in contrast to arc systems. Pressure, temperature and dissolved volatile content influence crystallization and hence magmatic evolution. Magmas stored at different depths or for different periods beneath a volcano will evolve along different paths (Andújar *et al.*, 2008; LeMasurier *et al.*, 2011; Andújar & Scaillet, 2012). Pre-eruptive evolution at or near the depth of H_2O saturation is the most important pre-conditioning factor (Andújar & Scaillet, 2012). This, along with the degrees of crystallinity, the viscosity of the melt phase and the total volatile content, controls the rate of bubble growth, coalescence and development of permeable networks to facilitate open-system degassing. Fluctuating magma ascent rates can also result in variations of eruption style within a single episode (Castro & Gardner, 2008). Understanding the workings of such magmatic systems will subsequently help forecast potential hazards in case of unrest.

Ulleung Island is an interesting location to study evolved alkalic eruptions, because it is a complex, long-lived, intraplate volcano that has been constructed by the emplacement of basaltic lavas and hyaloclastites, trachytic domes and lava flows, and also highly explosive caldera-forming eruptions of trachytic to phonolitic composition. The study described here has two principal objectives: (1) to investigate the relationship between eruptive style and pre-eruption magma storage conditions inferred from petrographic analysis and whole-rock geochemistry; (2) to gain insights into the processes and conditions controlling the evolution of trachytic and phonolitic magmas.

GEOLOGICAL SETTING AND SAMPLING OF ULLEUNG ISLAND

Ulleung Island is situated in the western East Sea/Sea of Japan, *c.* 130 km from the eastern shore of the Korean peninsula (Fig. 1a). It rises to 950 m a.s.l. from the *c.* 2000 m deep sea floor and is located at the northern margin of the Ulleung Basin, where this borders the South Korean continental plateau. Unlike the oceanic crust underlying the Japan Basin in the northeastern East Sea/Sea of Japan (Fig. 1a), the Ulleung Basin is founded on stretched continental crust, overlain by a thick succession of sedimentary and volcanic deposits (Tamaki *et al.*, 1992; Kim *et al.*, 2011). The crust in the middle of the Ulleung Basin is estimated at about 15 km thick, increasing to ~25 km at the margins (Kim *et al.*, 2003). The location of Ulleung Island at the northern edge of the Ulleung Basin corresponds to a crustal thickness of ~20 km.

Ulleung volcano has dated eruptions from 1·4 Ma until at least the middle Holocene (Kim *et al.*, 1999; Im *et al.*, 2012),

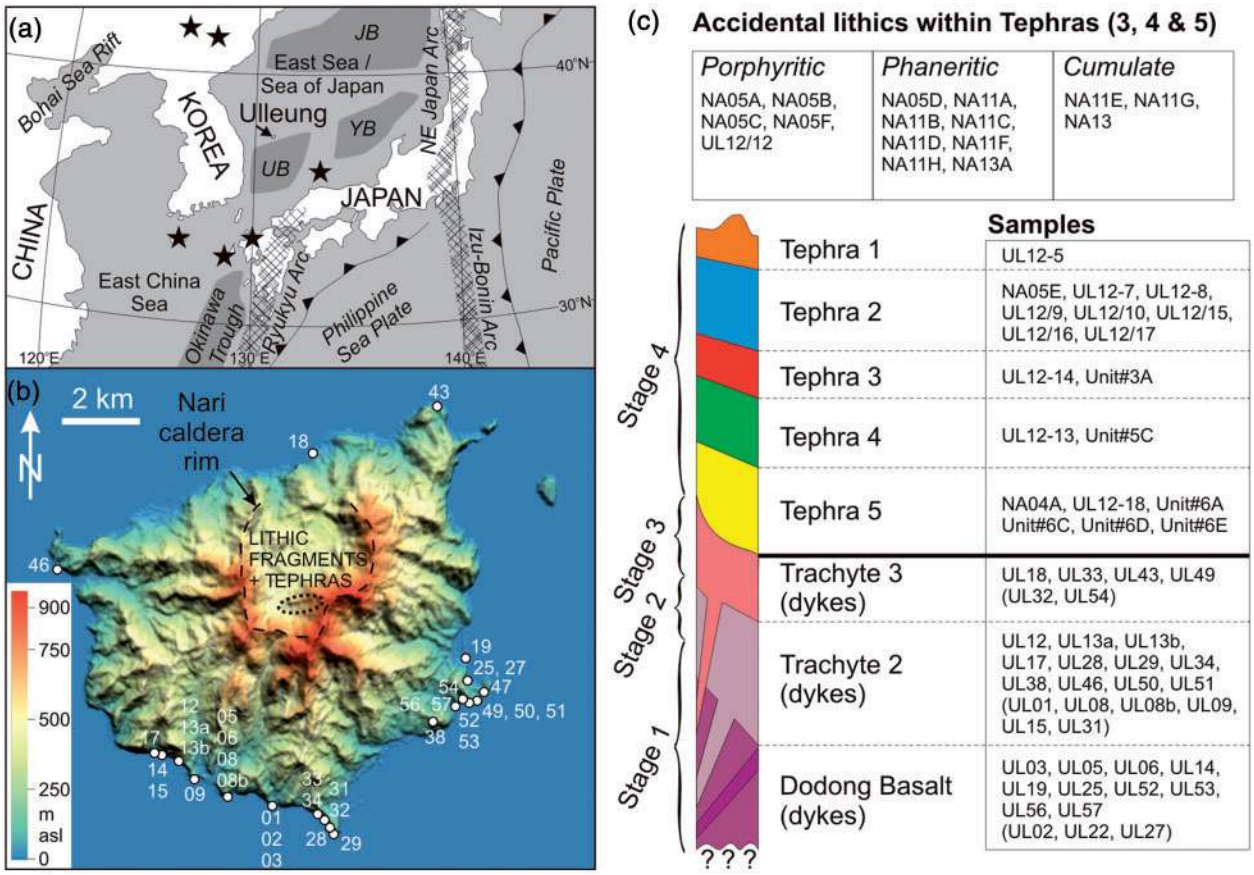

Fig. 1. (a) Geological setting and (b) digital elevation model (DEM) for Ulleung Island (950 m above sea level). Stars in (a) represent sites of Quaternary intraplate volcanic activity and cross-hatching indicates volcanic arcs. UB, YB and JB are the Ulleung, Yamato and Japan Basins. The JB is the only part of the East Sea/Sea of Japan to have experienced new oceanic crust formation, the rest being variously stretched continental blocks (Tamaki *et al.*, 1992). The numbers in (b) indicate locations of UL series whole-rock samples. The tephra samples and associated accidental lithics were collected within the dotted region inside the Nari caldera. (c) Schematic stratigraphic column (not to scale) and nomenclature with sample groupings; simplified after Kim *et al.* (1999).

and should therefore be considered as dormant. The history of the volcano has been subdivided into five stages, with basal basaltic lava and agglomerate capped by trachytic to phonolitic lavas and tephras (Kim, 1985; Kim *et al.*, 1999). We adopt a simplified classification in which Stages 4 and 5 of Kim *et al.* (1999) are grouped as Stage 4 (Fig. 1c), as they both belong to the caldera–post-caldera eruptive phase. The sequence of basaltic lavas and pyroclastic deposits of Stage 1 (referred to as Dodong Basalt, 1·37–0·97 Ma; Figs 1c and 2a, b) is locally tilted to 60–70° dipping seaward, but its basal contact is not exposed. The succession is intruded by several generations of basaltic dykes (here grouped within Stage 1) and trachytic dykes (generally <1 m thick; Fig. 2a) and locally by larger, trachyte bodies characterized by vertically fan-shaped flow structures (cryptodomes; Fig. 2c). In some cases cryptodomes have reached the surface to feed lava flows (Fig. 2d). These trachytes belong to Stages 2 (0·83–0·77 Ma) and 3 (0·73–0·24 Ma; Fig. 1c; Kim *et al.*, 1999). A series of caldera eruptions, which occurred *c.* 18·8, 8·4 and 5·6 ka BP, formed a circular depression (the Nari Basin) at the centre of the island (Im *et al.*, 2012) and deposited a thick tephra succession (Stage 4; Fig. 2e and f). Tephra fall from these eruptions has been detected in central Japan (Machida & Arai, 1983; Park *et al.*, 2003). An early survey (Tsuboi, 1920) described the presence of leucite-bearing trachyandesite lava and spatter related to post-caldera activity within the crater, and these correlate to our Tephra 1 (Stage 4).

The caldera-forming eruptions carried to the surface abundant lithic fragments of coarse-grained igneous material, which have been previously classified as gabbroic, monzonitic and syenitic based on modal mineralogy (Kim & Fujimaki, 1987; Kim *et al.*, 2008). These, together with the volcanic products, were previously employed to develop petrogenetic models involving fractional crystallization with variable amounts of crustal assimilation to account for chemical variability from basalts–trachybasalt to trachyte and phonolite (Kim, 1986; Kim *et al.*, 1999, 2008). However, the chemical variability within the

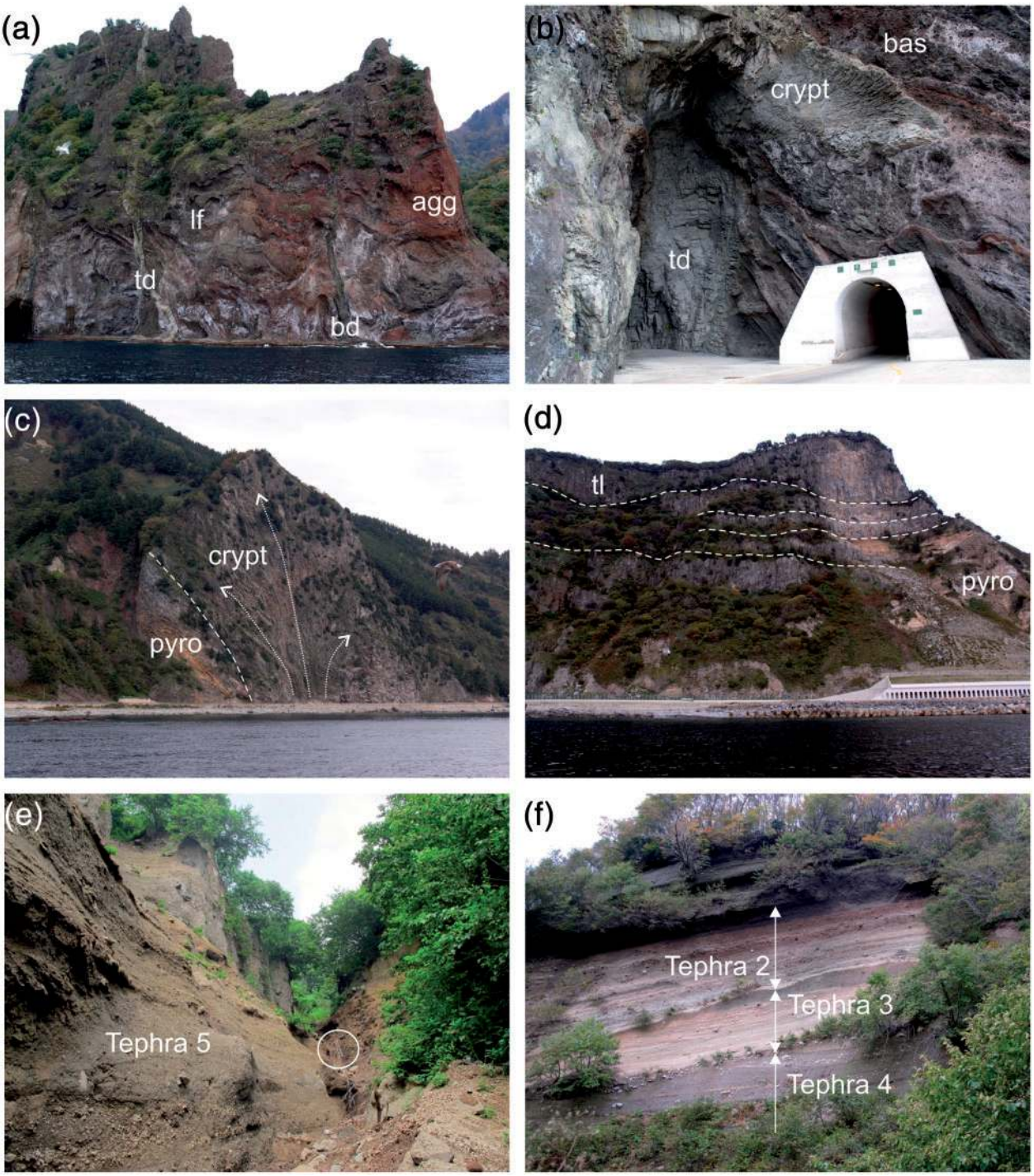

Fig. 2. (a) The Dodong Basalt consists of successions of thin lavas flows (lf), lava tongues and agglomerate (agg) intruded by trachybasaltic (bd) and trachytic dykes (td); height of cliff 25 m. (b) Locally trachytic dykes (td) expand laterally through the basaltic (bas) succession and feed cryptodomes (crypt). (c) Given sufficient magma supply these cryptodomes (crypt) breach the surface, here through a pyroclastic succession (pyro); height of cliff 100 m. (d) A stack of trachytic lavas (tl) interbedded with reworked and pyroclastic deposits (pyro). (e) Outcrop of Tephra 5 in a gully inside the Nari Caldera, ladder (circled) for scale. (f) Tephras 4, 3 and 2; the erosional surfaces between the units should be noted; height of cliff *c.* 40 m.

evolved part of the suite (trachyte–phonolite) is not completely explained by these models.

Our study is based on 71 samples collected from outcrops of the Dodong Basalt (Stage 1), from trachytic lava flows and domes (Stages 2 and 3), from dykes intruding both these rock units and belonging to these stages, and from pyroclastic successions within the Nari caldera (Fig. 1b). Additionally, a suite of samples, representing lithic fragments brought to the surface by the caldera-forming eruptions, was collected from a stream that cuts through the thickest pyroclastic succession in the Nari caldera. These are classified as phaneritic (fully crystalline), porphyritic (having phenocrysts in a very fine groundmass) or cumulate (crystalline assemblages of mainly mafic mineral phases) based on their texture (Fig. 1c).

PETROGRAPHY AND MINERAL CHEMISTRY

The following petrographic descriptions are organized on the basis of the total alkalis versus silica (TAS) chemical classification (Fig. 3a and b) of Le Bas *et al.* (1986). Three main volcanic and sub-volcanic rock types are represented in the surface samples: (1) trachybasaltic to basaltic trachyandesite lavas and dykes; (2) trachytic lava and dykes; (3) phonolitic pumice. Additionally, mafic cumulates, phaneritic rocks and samples with porphyritic textures occur in the suite of accidental lithics collected from intracaldera deposits of the Nari caldera (Stage 4).

Trachybasaltic to basaltic trachyandesite lavas and dykes are generally porphyritic (2–25% phenocrysts, with the lowest modal contents in vesiculated lavas) and characterized by euhedral to subhedral phenocrysts (1–5 mm) of olivine (<3%), clinopyroxene (5–10%), calcic plagioclase (10–15%) and magnetite (<3%) in a plagioclase, clinopyroxene and magnetite groundmass (<0·5 mm). Some olivine phenocrysts contain plagioclase and magnetite inclusions and many show alteration along fractures. Pseudomorphs of reddish brown iron oxide or cloudy brown clay after olivine are rare. Clinopyroxene phenocrysts are generally pale pinkish-brown in colour. They are commonly zoned and contain magnetite and plagioclase inclusions. Most plagioclase crystals are twinned, show oscillatory zoning and have intermediate (andesine) compositions. Lava samples are mostly vesicular. Vesicles are generally oval or spherical in shape and can reach several millimetres in size, but most are <5 mm in diameter.

Trachytic lavas and dykes are generally porphyritic (5–40% phenocrysts) and flow textured. Phenocrysts (1–10 mm) are usually euhedral to subhedral and include alkali feldspar (10–20%), which also forms glomerocrysts, clinopyroxene (<5%) and, less commonly olivine, biotite and plagioclase in an alkali feldspar and clinopyroxene groundmass (<0·5 mm) with minor apatite and disseminated Fe–Ti oxides. Alkali feldspar is simply twinned, whereas plagioclase is multiply (albitic) twinned and shows oscillatory zoning. Clinopyroxene phenocrysts are generally pale green in colour and some crystals have brown–green cores and contain magnetite inclusions. Olivine is rare and occurs as embayed anhedral phenocrysts surrounded by coronae of microcrystalline biotite and amphibole. Brown biotite (α = pale straw, $\beta = \gamma$ = dark chocolate brown) phenocrysts (<2 mm) are either fresh or completely replaced by black Fe–Ti oxides, although the characteristic cleavage is commonly preserved. Dykes tend to be finer grained with phenocrysts <3 mm.

Accidental lithics with porphyritic textures, collected within the Nari intracaldera sequence, differ from the other trachyte samples collected around Ulleung Island in containing amphibole. This is brownish green (α = pale green–brown, β = green–brown, γ = very dark green–brown) when subhedral and reddish brown (α = straw yellow, β = pale reddish brown, γ = deep reddish brown) when anhedral and partially resorbed, with dark biotite (α = pale brown, $\beta = \gamma$ = very dark chocolate brown) reaction rims. These samples also contain a variety of feldspar textures, such as perthite exsolution lamellae in some large (10 mm) phenocrysts, as well as single crystals or glomerocrystic aggregates with coronae of biotite.

Phonolitic pumices contain euhedral to subhedral phenocrysts (5–20%) of alkali feldspar (10–15%), green clinopyroxene (4%), brown amphibole (<2%; α = pale yellow, β = reddish brown, γ = dark chocolate brown), brown biotite (<2%; α = pale brown, $\beta = \gamma$ = very dark chocolate brown), plagioclase (<2%) and minor Fe–Ti oxides in a glassy, highly vesiculated (30–60%) groundmass. Euhedral to subhedral alkali feldspar phenocrysts are generally not twinned or zoned, but alkali feldspar and plagioclase forming glomerocrysts show twinning and zoning and crystals in these aggregates contain biotite inclusions. Subhedral green clinopyroxene occurs in some cases as an intergrowth with biotite. Subhedral amphibole phenocrysts contain inclusions of apatite and Fe–Ti oxides. The vesicles (generally <1 mm) are rounded to stretched and flow banding is defined by domains of collapsed vesicularity but similar mineral assemblages. Biotite and amphibole are commonly surrounded by 0·1 mm micro-vesicular and microlitic rims. Some tephras contain glomerocrystic aggregates with a texture resembling that of phaneritic accidental lithics.

The phaneritic lithics suite samples consist of assemblages of alkali feldspar, amphibole, clinopyroxene and biotite with minor disseminated Fe–Ti oxides and apatite. Feldspathoids (nepheline, sodalite), plagioclase and titanite are rare. Crystal size ranges from 0·3 to 5 mm (average of 2 mm) with the minor phases having grain sizes <0·1 mm.

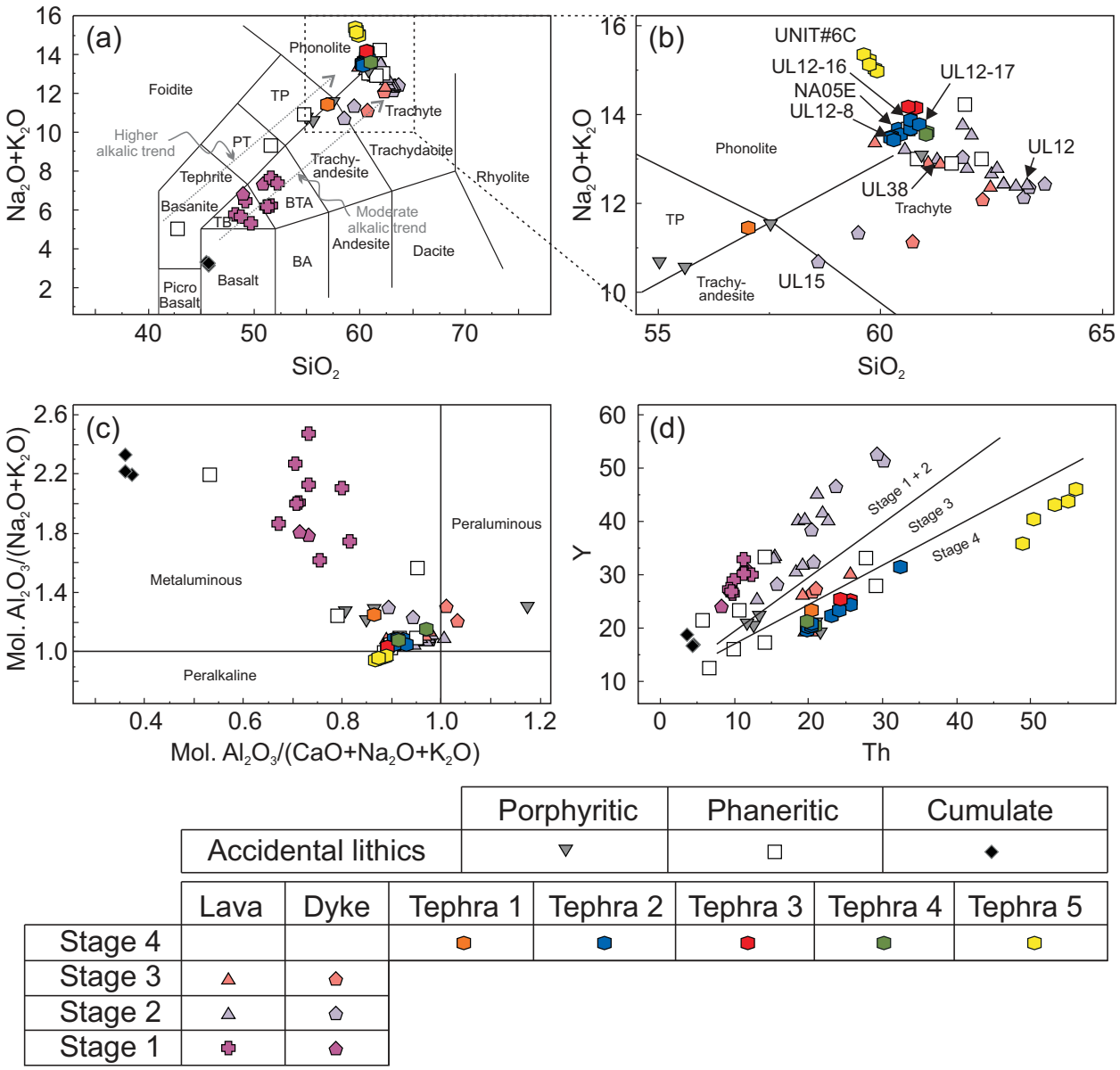

Fig. 3. Chemical classification of the Ulleung sample suite. (a) Total alkalis vs silica (TAS) classification (Le Bas *et al.*, 1986); TP, tephriphonolite; PT, phonotephrite; TB, trachybasalt; BTA, basaltic trachyandesite; BA, basaltic andesite. The phaneritic lithics and mafic cumulate lithics are plotted for comparison; however, the TAS effusive nomenclature does not apply to them. (b) Enlargement of (a) in the trachyte–phonolite region. (c) Peralkalinity index. (d) Distinction of the chemical stages at Ulleung based on degrees of Y enrichment. The samples numbered in (b) are used for the fractionation models (Table 10). (See text for details.)

Alkali feldspar forms 60–85% of the mode of most syenites and varies from fresh to altered (to dusty clays). Inclusions of Fe–Ti oxides and plagioclase are common in larger feldspar grains. Clinopyroxene (2–15%) is generally dark green or pale green with brown cores and overgrowths or replacement rims of brown amphibole (α = pale brown, β = reddish brown, γ = dark chocolate brown). Amphibole (1–10%) is subhedral to anhedral and interstitial; it contains apatite and Fe–Ti inclusions and forms intergrowths with feldspars. Fresh, brown biotite (up to 5%; α = pale brown, $\beta = \gamma$ = dark chocolate brown) commonly contains apatite inclusions and forms anhedral to subhedral intergrowths with amphibole. Plagioclase, where present, forms subhedral, interstitial or intergrown crystals <2 mm in size, which generally show lamellar twinning. Titanite generally forms anhedral grains up to 1 mm in size. Sample NA11D (compositionally a phonolite, but coarse-grained crystalline) has very small patches of interstitial glass within the main alkali feldspar framework and these contain fine (<50 μm) vesicles.

The apparent order of crystallization is alkali feldspar + clinopyroxene + amphibole + Fe–Ti oxide, followed by biotite + apatite + titanite.

Mafic cumulates are coarse grained and consist of clinopyroxene, olivine and magnetite with interstitial plagioclase, alkali feldspar, biotite and accessory apatite. Grain size ranges up to 10 mm but averages 3–5 mm. Clinopyroxene forms 50–60% of the typical mafic cumulate and occurs as euhedral to subhedral, zoned grains, light pinkish in colour with colourless cores and abundant magnetite inclusions. Some grains show patchy alteration to brown biotite. Subhedral olivine (10%) is generally slightly altered along fractures to opaque minerals or dusty clays and is rarely observed as inclusions in clinopyroxene. Biotite (10–15%) occurs as both yellowish brown (α = straw yellow, $\beta = \gamma$ = dark chocolate brown) subhedral grains and reddish brown (α = pale brown, $\beta = \gamma$ = reddish brown) anhedral disseminated flakes rimming olivine crystals. Magnetite occurs as anhedral disseminated grains up to 0·6 mm in size with well-developed ilmenite exsolution lamellae. The intercumulus (30%) assemblage ranges in size from 0·5 to 3 mm, and consists of intergrowths of lamellar twinned plagioclase showing pervasive sericitization (20–25%) with minor light pink or green clinopyroxene, flaky biotite and magnetite. Cumulate olivine magnetite and clinopyroxene crystallized first and were followed by intercumulus plagioclase and alkali feldspar, clinopyroxene, magnetite and biotite.

Mineral chemistry

The principal mineral phases have been analysed in representative samples of each of the main rock types. Mineral analyses were obtained by electron microprobe using a JEOL JXA-8100 at Gyeongsang National University, South Korea. Standard operating conditions for wavelength dispersive spectroscopy (WDS) used for all measurements were an accelerating voltage of 15 kV, beam current of 0·2 nA and beam diameter of 10 μm. Analytical precision was estimated by replicate analyses of mineral standards as (σ) ≤3% for elements present in abundances >1 wt %. Representative compositions are reported in Tables 1–6 and the whole dataset is available in Supplementary Data Electronic Appendix 1 (supplementary data are available for downloading at http://www.petrology.oxfordjournals.org).

Olivine (Table 1) is common in the trachybasalt–basaltic trachyandesite (Dodong Basalt) and the mafic cumulates samples, but is rare in the more evolved rock units, where, if present, it generally shows disequilibrium or reaction textures such as embayments and coronae of biotite–amphibole. Fo# content is between 70 and 83 in olivine from the Dodong Basalt and mafic cumulate accidental lithics, but 86–87 in olivines in the trachytic rocks.

Pyroxenes (Table 2) are mostly diopsidic clinopyroxene (Fig. 4a) although one sample from the phaneritic accidental lithic suite (NA11D) contains green sodic hedenbergite (1·0–2·6 wt % Na_2O, Fig. 4c; Morimoto *et al.*, 1988). The accidental porphyritic lithic sample NA05B (trachyandesite) contains clinopyroxene cores rich in MgO and TiO_2 (Fig. 4b and c) rimmed by oscillatory zoned diopsidic pyroxene.

Amphibole (Table 3) is mainly kaersutite although the TiO_2 (2–6·5 wt %) and especially MgO (5–13 wt %) and FeO (9–23 wt %) contents can vary considerably and hence some analysed grains are more accurately classified as ferrokaersutite (Leake *et al.*, 1997). Samples of the phaneritic accidental lithic suite contain both kaersutite and ferrokaersutite, whereas in Stage 4 phonolitic pumices ferrokaersutite (2–3 wt % TiO_2; 4–6 wt % MgO; 23–26 wt % FeO) occurs in Tephra 5 and kaersutite (5–6 wt % TiO_2; 11–13 wt % MgO; 9–11 wt % FeO) in Tephra 1 and 2.

Table 1: Representative electron microprobe analyses of olivine

Analysis:	126	115	203	184
Sample:	UL27	NA05B	NA11E	NA11E
Stage:	1	PO	CM	CM
SiO_2	38·13	40·60	39·82	40·16
TiO_2	b.d.l.	0·02	b.d.l.	b.d.l.
Al_2O_3	0·06	0·02	b.d.l.	0·01
FeO	22·85	12·13	16·96	18·29
MnO	0·44	0·17	0·33	0·25
MgO	38·60	47·54	44·21	42·65
CaO	0·19	0·26	0·25	0·27
Na_2O	0·02	b.d.l.	0·02	0·02
K_2O	0·03	0·02	b.d.l.	b.d.l.
Cr_2O_3	b.d.l.	0·09	0·01	b.d.l.
Total	100·33	100·85	101·60	101·65
Cations on the basis of 4 O				
Si	0·99	1·00	0·99	1·01
Ti	0·00	0·00	0·00	0·00
Al	0·00	0·00	0·00	0·00
Fe	0·50	0·25	0·35	0·38
Mn	0·01	0·00	0·01	0·01
Mg	1·50	1·74	1·64	1·59
Ca	0·01	0·01	0·01	0·01
Na	0·00	0·00	0·00	0·00
K	0·00	0·00	0·00	0·00
Cr	0·00	0·00	0·00	0·00
Total	3·01	3·00	3·01	2·99
Fo#	0·75	0·87	0·82	0·81

b.d.l., below detection limit; PO, porphyritic lithic; CM, mafic cumulate lithic.

Table 2: Representative electron microprobe analyses of clinopyroxene

Analysis:	206	8	282	134	72	327	65
Sample:	UL12-5	UL12-9	UL09	UL27	UL28	UL35	NA05E
Stage:	4 Tephra 1	4 Tephra 2	2	1	2	1	4 Tephra 2
SiO_2	49·97	50·56	51·30	48·15	51·67	46·08	49·47
TiO_2	0·88	0·79	0·28	2·42	0·58	2·76	1·14
Al_2O_3	2·64	2·29	0·69	6·31	1·29	8·63	3·05
FeO	12·70	13·21	18·48	7·03	10·07	7·40	12·30
MnO	0·75	0·78	1·47	0·11	0·96	0·11	0·68
MgO	10·38	9·84	6·88	13·38	12·67	12·54	10·25
CaO	21·91	21·57	20·73	21·92	21·34	21·85	21·78
Na_2O	0·76	0·78	0·58	0·52	0·56	0·54	0·82
K_2O	b.d.l.	0·01	b.d.l.	0·01	0·01	0·01	0·01
Cr_2O_3	0·02	b.d.l.	b.d.l.	0·00	b.d.l.	0·05	b.d.l.
Total	99·99	99·81	100·40	99·85	99·15	99·97	99·49
Cations on the basis of 6 O							
Si	1·91	1·94	2·00	1·79	1·96	1·72	1·90
Ti	0·03	0·02	0·01	0·07	0·02	0·08	0·03
Al	0·12	0·10	0·03	0·28	0·06	0·38	0·14
Fe	0·41	0·42	0·60	0·22	0·32	0·23	0·39
Mn	0·02	0·03	0·05	0·00	0·03	0·00	0·02
Mg	0·59	0·56	0·40	0·74	0·72	0·70	0·59
Ca	0·90	0·89	0·87	0·88	0·87	0·88	0·90
Na	0·06	0·06	0·04	0·04	0·04	0·04	0·06
K	0·00	0·00	0·00	0·00	0·00	0·00	0·00
Cr	0·00	0·00	0·00	0·00	0·00	0·00	0·00
Total	4·03	4·02	4·00	4·02	4·01	4·03	4·03
En	30·82	29·64	20·86	40·38	37·05	38·62	30·87
Fs	22·42	23·65	33·97	12·09	18·11	12·99	21·95
Wo	46·77	46·71	45·17	47·53	44·85	48·39	47·17

Analysis:	381	107	25	33	212	198
Sample:	NA05A	NA05B	NA11D	NA11D	NA11E	NA11E
Stage:	PO	PO	PH	PH	CM	CM
SiO_2	52·03	47·54	48·46	48·56	48·79	52·67
TiO_2	0·59	2·23	0·75	0·66	2·36	0·84
Al_2O_3	4·10	6·62	2·29	1·96	5·35	3·20
FeO	4·82	6·94	19·79	22·10	6·78	4·37
MnO	0·09	0·16	1·58	2·44	0·11	0·09
MgO	16·21	13·85	4·58	2·33	13·81	16·30
CaO	21·43	21·68	20·91	19·33	22·13	21·90
Na_2O	0·37	0·54	1·21	2·32	0·46	0·38
K_2O	0·01	b.d.l.	0·03	0·00	b.d.l.	0·03
Cr_2O_3	0·30	b.d.l.	0·03	0·01	0·02	0·42
Total	99·96	99·55	99·62	99·69	99·80	100·21

(continued)

Table 2: Continued

Analysis:	381	107	25	33	212	198
Sample:	NA05A	NA05B	NA11D	NA11D	NA11E	NA11E
Stage:	PO	PO	PH	PH	CM	CM
Cations on the basis of 6 O						
Si	1·90	1·78	1·93	1·96	1·82	1·92
Ti	0·02	0·06	0·02	0·02	0·07	0·02
Al	0·18	0·29	0·11	0·09	0·23	0·14
Fe	0·15	0·22	0·66	0·75	0·21	0·13
Mn	0·00	0·01	0·05	0·08	0·00	0·00
Mg	0·88	0·77	0·27	0·14	0·77	0·89
Ca	0·84	0·87	0·89	0·84	0·88	0·86
Na	0·03	0·04	0·09	0·18	0·03	0·03
K	0·00	0·00	0·00	0·00	b.d.l.	0·00
Cr	0·01	0·00	0·00	0·00	0·00	0·01
Total	4·00	4·03	4·04	4·06	4·02	4·00
En	47·16	41·46	14·49	7·77	41·13	47·19
Fs	8·02	11·92	37·97	45·93	11·51	7·25
Wo	44·82	46·63	47·54	46·30	47·36	45·57

PH, phaneritic lithic.

Biotite (Table 4) is a common phase in both trachytic and phonolitic rocks, as well as the phaneritic and mafic cumulate accidental lithics. The composition is generally biotite in the strict sense (Bailey, 1984) but all analysed biotite is relatively rich in TiO_2 (5·5–8·5 wt %) and the ratio of MgO and FeO is variable. The Mg# is between 60 and 70 in biotites from the mafic cumulates, but generally lower (between 40 and 55 and as low as 30) in some phaneritic accidental lithic samples.

Feldspar (Table 5, Fig. 5) compositions in the Ulleung rocks cover the entire spectrum from bytownite through albite to orthoclase. Feldspars in the mafic cumulate accidental lithics have compositions between An_{80} and An_{12} and $Or_{<5}$. The Stage 1 lavas and dykes mostly contain plagioclase with $An_{60–80}$. Samples from trachyte flows and domes, as well as trachytic dykes (Stages 2 + 3), contain alkali feldspars with $Or_{25–55}$ and $An_{<10}$. Two porphyritic accidental lithics collected from the Nari stream (NA05A and B, both close to the tephriphonolite–trachyandesite boundary) contain feldspars with compositions covering almost the entire spectrum from An_{62} to Or_{85} (Fig. 5). In these samples the crystals commonly show disequilibrium features such as rounded edges and coronae of biotite, or they occur as glomerocrysts with different textures and compositions indicating that they may be of xenocrystic origin. Samples from the syenitic suite are mostly alkali feldspars with $Or_{40–50}$ although crystals with compositions in the range $Or_{10–20}$ and $An_{<3}$, and $An_{20}Ab_{70}Or_{10}$ also

Table 3: Representative electron microprobe analyses of amphibole

Analysis:	107	122	106	85	370	103	104	403
Sample:	UL12-18	UL12-18	UL12-18	NA05E	NA05A	NA05B	NA05B	NA11B
Stage:	4 Tephra 5	4 Tephra 5	4 Tephra 5	4 Tephra 2	PO	PO	PO	PH
SiO_2	38·98	37·93	39·59	38·91	39·49	38·22	35·16	39·85
TiO_2	4·06	2·89	4·42	5·97	6·42	6·34	5·20	2·32
Al_2O_3	11·40	11·27	11·49	12·88	14·23	14·42	14·50	11·62
FeO	22·99	29·70	20·67	11·50	10·23	9·63	22·63	23·06
MnO	0·94	1·61	0·78	0·19	0·10	0·12	0·62	0·97
MgO	4·98	0·94	6·57	11·67	12·39	12·77	8·06	5·57
CaO	11·20	10·46	11·15	11·97	12·24	11·89	0·05	10·84
Na_2O	2·42	2·49	2·12	2·35	2·16	2·15	0·31	2·85
K_2O	1·76	1·70	1·89	1·68	1·55	1·59	9·44	1·69
Cr_2O_3	0·03	b.d.l.	b.d.l.	b.d.l.	b.d.l.	b.d.l.	b.d.l.	0·04
Total	98·76	98·98	98·67	97·11	98·81	97·12	95·96	98·81
Cations on the basis of 23 O								
Si	6·09	6·12	6·11	5·85	5·78	5·69	5·71	6·21
Ti	0·48	0·35	0·51	0·67	0·71	0·71	0·64	0·27
Al	2·10	2·14	2·09	2·28	2·45	2·53	2·78	2·13
Fe	3·00	4·01	2·67	1·45	1·25	1·20	3·07	3·00
Mn	0·12	0·22	0·10	0·02	0·01	0·02	0·08	0·13
Mg	1·16	0·23	1·51	2·62	2·70	2·83	1·95	1·29
Ca	1·88	1·81	1·84	1·93	1·92	1·90	0·01	1·81
Na	0·73	0·78	0·63	0·68	0·61	0·62	0·10	0·86
K	0·35	0·35	0·37	0·32	0·29	0·30	1·96	0·34
Cr	0·00	0·00	0·00	0·00	0·00	0·00	0·00	0·00
Total	15·92	16·02	15·84	15·83	15·74	15·80	16·29	16·05

occur. The feldspars in Stage 4 phonolitic tephra samples have a bimodal compositional distribution. Most feldspar phenocrysts have compositions in the range $Or_{50–65}$ but some samples contain plagioclase with albite twins and compositions in the range $An_{15–50}$. These samples also have the most extensive ternary solid solution range of all the Ulleung feldspars with one composition being $An_{20}Ab_{65}Or_{15}$ (Fig. 5).

Iron–titanium oxides (Table 6) are titanomagnetite (solid solution of magnetite and ulvöspinel) and ilmenite. Ilmenite commonly forms exsolution lamellae in titanomagnetite grains. However, two samples contain intergrown titanomagnetite and ilmenite embedded in clinopyroxene phenocrysts, which suggests that in this particular case the two oxides were in equilibrium before entrainment into the host silicate mineral.

Minerals present in minor or trace amounts include sodalite, nepheline (Table 5), apatite, titanite and a Nb–Zr oxide tentatively identified as marianoite or whölerite. With the exception of apatite these accessory minerals are most common in phaneritic accidental lithic samples. Nepheline from sample NA11C (phaneritic accidental lithic on the tephriphonolite–trachyandesite boundary) has been analysed and its composition plots on or close to the 775°C isotherm in the ternary system SiO_2–$NaAlSiO_4$–$KAlSiO_4$ based on the experimental work of Hamilton (1961; Fig. 6).

WHOLE-ROCK GEOCHEMISTRY

Analytical procedure

Clean rock specimens were crushed between tungsten carbide plates and clean chips were handpicked and milled in a tungsten carbide ring grinder. H_2O and loss on ignition (LOI) were measured by heating ~4 g of sample for 12 h at 105°C and 1000°C respectively. Two grams of dried sample powder were weighed together with 6 g of SPECTRACHEM 12-22 flux and the mixture was fused in Pt crucibles and moulded and cooled into a glass disc. Major element concentrations were measured by X-ray

Table 4: Representative electron microprobe analyses of biotite

Analysis:	192	14	300	81	126	83	398	209
Sample:	UL12-5	UL12-9	UL09	UL28	NA05B	NA05E	NA11B	NA11E
Stage:	4 Tephra 1	4 Tephra 2	2	2	PO	4 Tephra 2	PH	CM
SiO_2	35·09	35·67	36·24	36·80	36·02	35·56	35·96	37·14
TiO_2	7·79	7·76	5·51	8·01	6·21	7·32	4·45	7·10
Al_2O_3	14·75	14·36	13·25	13·63	14·34	13·95	13·71	14·53
FeO	18·69	19·29	21·99	16·95	21·47	19·81	25·14	13·75
MnO	0·35	0·22	0·49	0·42	0·32	0·37	0·80	0·12
MgO	10·70	10·66	8·69	11·64	9·30	9·68	7·76	14·17
CaO	0·02	0·00	b.d.l.	0·03	0·00	0·01	0·01	0·03
Na_2O	0·66	0·74	0·68	0·88	0·73	0·71	0·56	0·74
K_2O	9·08	9·10	8·82	8·81	8·83	9·22	8·97	8·89
Cr_2O_3	0·03	0·04	0·01	b.d.l.	0·05	b.d.l.	0·03	0·00
Total	97·14	97·85	95·69	97·16	97·26	96·64	97·37	96·47
Cations on the basis of 22 O								
Si	5·28	5·33	5·60	5·47	5·46	5·41	5·56	5·45
Ti	0·88	0·87	0·64	0·89	0·71	0·84	0·52	0·78
Al	2·61	2·53	2·42	2·39	2·56	2·50	2·50	2·52
Fe	2·35	2·41	2·84	2·11	2·72	2·52	3·25	1·69
Mn	0·04	0·03	0·06	0·05	0·04	0·05	0·10	0·01
Mg	2·40	2·37	2·00	2·58	2·10	2·19	1·79	3·10
Ca	0·00	0·00	0·00	0·00	0·00	0·00	0·00	0·00
Na	0·19	0·21	0·20	0·25	0·22	0·21	0·17	0·21
K	1·74	1·74	1·74	1·67	1·71	1·79	1·77	1·67
Cr	0·00	0·01	0·00	0·00	0·01	0·00	0·00	0·00
Total	15·50	15·50	15·52	15·41	15·51	15·51	15·65	15·44
Mg#	0·50	0·50	0·41	0·55	0·44	0·47	0·35	0·65

fluorescence (XRF; Siemens SR3000 spectrometer) at the University of Auckland. Major and minor elements (Si, Ti, Al, Fe, Mn, Mg, Ca, Na, K, P) were determined as oxide components using methods similar to those described by Norrish & Hutton (1969). In general, precision for each major or minor element is better than ±1% (1σ) of the reported value. Fe was measured as total Fe_2O_3 and analyses were recalculated to 100% volatile free and total FeO. Additionally, we report XRF Pb concentrations. These were measured on the same glass disks as for the major elements with a suite of 36 international standards used for calibration and Siemens SPECTRA 3000 software used for data reduction. The Compton scatter of X-ray tube RhKbl emission was used to correct for mass attenuation. Theoretical detection limit is 1–2 ppm and reproducibility is <5% (2σ). Representative major element analyses are reported in Table 7 and the whole dataset is available in Supplementary Data Electronic Appendix 2.

Trace elements were measured by laser ablation inductively coupled plasma mass spectrometry (LA-ICP-MS, except for Pb) at the Research School of Earth Sciences, Australian National University, using an Excimer LPX120 laser (193 nm) and Agilent 7500 series mass spectrometer, following the method of Eggins *et al.* (1998). For this work, the same fused glass discs as for XRF were prepared as a multi-sample polished mount. Samples were run in batches of 15 using NST612 glass standard at the beginning and end of each run to calibrate. Standard BCR-2 was also run with each batch to monitor analytical performance. Repeat analyses of standard BCR-2 indicate precision of <4% (RSD) and accuracy better than 5% at the 95% confidence level for most elements. Representative trace element concentrations are reported in Table 8 and the complete dataset including data for standard rocks is available as Supplementary Data Electronic Appendix 2.

Table 5: Representative electron microprobe analyses of feldspar and nepheline

Analysis:	193	227	23	150	105	104	272
Sample:	UL12-5	UL12-5	UL12-9	UL12-17	UL12-18	UL12-18	UL09
Stage:	4 Tephra 1	4 Tephra 1	4 Tephra 2	4Tephra 2	4 Tephra 5	4 Tephra 5	2
SiO_2	54·92	64·38	59·65	64·71	64·71	64·94	66·43
TiO_2	0·03	0·08	0·06	0·02	0·07	0·01	0·00
Al_2O_3	27·97	19·73	24·76	19·75	19·76	19·51	19·55
FeO	0·31	0·15	0·29	0·12	0·14	0·10	0·12
MnO	b.d.l.	b.d.l.	0·03	0·05	b.d.l.	b.d.l.	0·05
MgO	b.d.l.	b.d.l.	0·00	b.d.l.	b.d.l.	b.d.l.	b.d.l.
CaO	10·14	0·74	6·34	0·63	0·73	0·81	0·74
Na_2O	5·25	3·71	6·79	4·42	4·75	4·59	6·57
K_2O	0·85	10·67	1·51	10·06	9·69	9·78	7·08
Cr_2O_3	0·02	0·02	b.d.l.	0·01	0·01	b.d.l.	0·03
Total	99·47	99·48	99·43	99·76	99·85	99·74	100·57
Cations on the basis of 8 O							
Si	2·49	2·94	2·68	2·94	2·94	2·95	2·96
Ti	0·00	0·00	0·00	0·00	0·00	0·00	0·00
Al	1·50	1·06	1·31	1·06	1·06	1·05	1·03
Fe	0·01	0·01	0·01	0·00	0·01	0·00	0·00
Mn	0·00	0·00	0·00	0·00	0·00	0·00	0·00
Mg	0·00	0·00	0·00	0·00	0·00	0·00	0·00
Ca	0·49	0·04	0·31	0·03	0·04	0·04	0·04
Na	0·46	0·33	0·59	0·39	0·42	0·40	0·57
K	0·05	0·62	0·09	0·58	0·56	0·57	0·40
Cr	0·00	0·00	0·00	0·00	0·00	0·00	0·00
Total	5·01	5·00	5·00	5·01	5·02	5·01	5·01
An	49·11	3·66	31·03	3·05	3·48	3·90	3·51
Ab	45·99	33·29	60·15	38·80	41·21	39·99	56·47
Or	4·90	63·06	8·82	58·15	55·31	56·11	40·02

Analysis:	137	75	347	125	129	21	228	3847
Sample:	UL27	UL28	UL35	NA05B	NA05B	NA11D	NA11E	NA11C
Stage:	1	2	2	PO	PO	PH	PH	PH
SiO_2	50·93	65·37	50·05	67·00	43·86	66·24	63·98	44·78
TiO_2	0·06	0·08	0·09	b.d.l.	3·64	0·02	0·01	0·01
Al_2O_3	30·90	19·34	31·49	19·56	9·87	18·84	23·05	32·37
FeO	0·42	0·20	0·44	0·12	6·76	0·21	0·20	0·33
MnO	0·05	0·01	b.d.l.	0·05	0·13	b.d.l.	0·03	0·01
MgO	0·05	b.d.l.	0·09	b.d.l.	12·07	b.d.l.	0·01	b.d.l.
CaO	13·57	0·76	14·41	0·40	22·22	0·11	4·02	0·29
Na_2O	3·23	5·42	2·84	5·77	0·51	5·77	8·62	16·33
K_2O	0·45	8·35	0·41	8·84	0·03	8·46	0·72	4·79
Cr_2O_3	0·01	0·02	b.d.l.	b.d.l.	b.d.l.	0·03	b.d.l.	0·07
Total	99·66	99·53	99·83	101·74	99·08	99·69	100·63	99·31

(continued)

Table 5: Continued

Analysis:	137	75	347	125	129	21	228	3847
Sample:	UL27	UL28	UL35	NA05B	NA05B	NA11D	NA11E	NA11C
Stage:	1	2	2	PO	PO	PH	PH	PH
Cations on the basis of 8 O (32 for nepheline 3847)								
Si	2·33	2·96	2·29	2·97	2·21	2·99	2·81	8·58
Ti	0·00	0·00	0·00	0·00	0·14	0·00	0·00	0·00
Al	1·66	1·03	1·70	1·02	0·59	1·00	1·19	7·30
Fe	0·02	0·01	0·02	0·00	0·28	0·01	0·01	0·06
Mn	0·00	0·00	0·00	0·00	0·01	0·00	0·00	0·00
Mg	0·00	0·00	0·01	0·00	0·91	0·00	0·00	0·00
Ca	0·66	0·04	0·71	0·02	1·20	0·01	0·19	0·06
Na	0·29	0·48	0·25	0·50	0·05	0·51	0·73	6·05
K	0·03	0·48	0·02	0·50	0·00	0·49	0·04	1·18
Cr	0·00	0·00	0·00	0·00	0·00	0·00	0·00	0·00
Total	4·99	5·00	5·00	5·02	5·38	5·00	4·98	23·30
An	68·03	3·71	71·89	1·89	95·88	0·55	19·63	(Q) 7·17
Ab	29·32	47·81	25·68	48·85	3·98	50·62	76·20	(Ne) 76·22
Or	2·65	48·48	2·43	49·26	0·14	48·83	4·17	(Ks) 16·61

Sr–Nd–Pb isotopic compositions were acquired at the University of Melbourne (Maas *et al.*, 2005). Acid-leached chips (6 M HCl, 100°C, 60 min), were dissolved (2 ml of 3:1 HF–HNO_3 for 2 days at 110°C and 6 M HCl for 1 day) on a hotplate, followed by sequential extraction of Pb, Sr and Nd using a combination of anion exchange and EICHROM RE, LN and SR resin chromatography. Blanks were <100 pg. Isotopic analyses were carried out on a NU Plasma multicollector (MC)-ICP-MS system. Sr and Nd isotope ratios were normalized to $^{86}Sr/^{88}Sr = 0{\cdot}1194$ and $^{146}Nd/^{145}Nd = 2{\cdot}0719425$ (equivalent to $^{146}Nd/^{144}Nd = 0{\cdot}7219$; Vance & Thirlwall, 2002), respectively, using the exponential law, and are reported relative to SRM987 = 0·710230 and La Jolla Nd = 0·511860. External precision (2σ) is ≤0·000040 for $^{87}Sr/^{86}Sr$ and ≤0·000020 for $^{143}Nd/^{144}Nd$. The results for international standards (BCR-2, BHVO-2, JNd-1) obtained in the course of this work (see Table 9) are consistent with reference data (Tanaka *et al.*, 2000; Raczek *et al.*, 2003; Elburg *et al.*, 2005; Weis *et al.*, 2006). Pb mass bias was corrected using the thallium-doping technique (Woodhead, 2002), which is expected to produce external precisions of 0·025–0·05% (2σ). High accuracy and precision are confirmed by the results for SRM981 and BCR-2 (see Table 9) and by repeated analyses of samples (not listed).

Major elements

The lithological groups used as the basis for the petrographic descriptions given above are also apparent in the major element chemistry (Figs 3 and 7). Samples collected from the Dodong Basalt (Stage 1) are generally trachybasalt to basaltic trachyandesite. Evolved lavas and pumices of Stages 2–4 define a trend from trachyte to phonolite. SiO_2 abundance varies from 43 to 64 wt %. This range extends to 43 wt % because of the sampled accidental lithics (phaneritic and cumulates). In the extrusive rocks, SiO_2 abundance ranges from 45 to 64 wt % with a gap between 53 and 58 wt %. A few dykes and the accidental lithics have compositions partially covering this gap (Figs 3 and 7). TiO_2, FeO, MgO and CaO abundances are negatively correlated with SiO_2 content, whereas Al_2O_3, Na_2O, K_2O and P_2O_5 abundances are positively correlated with SiO_2 content up to *c.* 55 wt % and are flat to weakly negatively correlated at >55 wt % SiO_2 (Fig. 7). The analysed accidental lithics from the Nari tephra sequence tend to have higher $Na_2O + K_2O$ and MgO abundances at comparable SiO_2 contents relative to the surface samples or the dykes and therefore define a trend from basanite to tephriphonolite (the 'Higher alkalic trend' in Fig. 3a).

In contrast to the lava flows of Stages 2 and 3, which are trachytic, the tephra samples of Stage 4 are phonolitic; that is, they are richer in $Na_2O + K_2O$ (Fig. 3a and b). They additionally define a trend towards peralkalinity as opposed to a trend towards the peraluminous compositions of the trachytes (Fig. 3c). Most samples are, however, metaluminous with mol. $Al_2O_3/(K_2O + Na_2O + CaO)$ between 0·3 and 1 and mol. $Al_2O_3/(K_2O + Na_2O)$ between 1 and

Table 6: Representative electron microprobe analyses of Fe–Ti oxides

Analysis:	358	363	139	140	152	115	63
Sample:	NA05A	NA05A	UL27	UL27	UL12-17	UL12-18	UL28
Stage:	PO	PO	1	1	4 Tephra 2	4 Tephra 5	2
SiO_2	b.d.l.	0·10	b.d.l.	0·04	0·08	0·10	0·04
TiO_2	5·83	48·25	47·02	17·03	19·54	19·29	20·55
Al_2O_3	4·50	0·13	0·67	6·39	2·41	1·66	1·72
FeO	82·38	47·25	40·90	65·61	71·88	73·09	69·03
MnO	0·41	1·41	0·49	0·51	1·46	2·03	2·10
MgO	0·33	0·95	7·62	6·70	1·51	0·60	2·16
CaO	b.d.l.	0·04	b.d.l.	0·00	0·01	0·01	0·01
Na_2O	0·06	b.d.l.	0·02	b.d.l.	b.d.l.	0·02	0·03
K_2O	b.d.l.	0·01	b.d.l.	b.d.l.	b.d.l.	b.d.l.	b.d.l.
Cr_2O_3	0·05	0·01	0·01	0·15	b.d.l.	0·02	b.d.l.
Total	93·57	98·13	96·73	96·43	96·90	96·83	95·63
Cations on the basis of 6 O (ilmenite) and 24 O (Ti-magnetite)							
Si	0·00	0·01	0·00	0·01	0·02	0·02	0·01
Ti	1·22	1·89	1·80	3·00	3·62	3·63	3·83
Al	1·47	0·01	0·04	1·77	0·70	0·49	0·50
Fe	19·10	2·06	1·74	12·85	14·81	15·29	14·32
Mn	0·10	0·06	0·02	0·10	0·30	0·43	0·44
Mg	0·14	0·07	0·58	2·34	0·56	0·22	0·80
Ca	0·00	0·00	0·00	0·00	0·00	0·00	0·00
Na	0·03	0·00	0·00	0·00	0·00	0·01	0·01
K	0·00	0·00	0·00	0·00	0·00	0·00	0·00
Cr	0·01	0·00	0·00	0·03	0·00	0·00	0·00
Total	22·06	4·10	4·18	20·09	20·01	20·11	19·91

2·3 and just three phonolite samples (Stage 4, Tephra 5) are classified as peralkaline with mol. $Al_2O_3/(K_2O + Na_2O) = 0·9$ (Table 7, Fig. 3c). A few samples are peraluminous with mol. $Al_2O_3/(K_2O + Na_2O + CaO) > 1$ (Fig. 3c). Other major components do not, however, show systematic variation with stratigraphic position. For example, Na_2O and K_2O abundances are not evenly distributed. Samples of Tephra 5 are richer in Na_2O and poorer in K_2O whereas the samples from Tephras 1, 2, 3 and 4 are richer in K_2O (Fig. 7g and h). Samples of Tephra 5 are almost completely depleted in TiO_2 and P_2O_5.

Trace elements

The abundances of large ion lithophile (LILE; e.g. Cs, Ba, Rb and Sr) and high field strength trace elements (HFSE; e.g. Nb, Th, U and Zr) and the REE (except for Eu^{2+}) are generally positively correlated with SiO_2 content up to 53 wt % (Stage 1 samples), but their behaviour in the evolved samples is variable. Thorium has been selected as an index of fractionation (Fig. 8) rather than SiO_2 because in some phonolite tephras the latter decreases with increasing degree of chemical evolution (Fig. 3b). Thorium abundance is positively correlated with SiO_2 content and it is linearly correlated through the origin with Zr content (Fig. 8a), an indication that it is incompatible in the majority of the sampled suites. The latter element could also be used as a fractionation index. However, given the presence of a Nb–Zr silicate phase in some rocks, Th is preferred. The abundances of trace elements compatible in mafic phases (Ni, Cr, Sc and V) and in feldspars (Sr and Ba) show a negative trend with increasing Th content (Fig. 8c and d) and all these elements are differently depleted in the trachytes and pumices of Stages 2–4. At comparable Th contents, Stage 4 phonolites retain Sr compared with the Stage 2 trachytes, whereas the latter are richer in Sc compared with the former (Fig. 8c and d).

Samples of the Dodong Basalt (Stage 1) have Nb/Zr between 0·20 and 0·30, similar to the range for trachyte and phonolite extrusive rocks (Fig. 8e). However, among the phaneritic lithic fragments the Nb/Zr ranges up to 0·50 in the most Th- and SiO_2-rich samples, and similar variation is observed among the porphyritic lithic fragments, with Nb/Zr ratio varying up to 0·35 (Fig. 8e). Whole-rock samples of Ulleung alkalic extrusive rocks analysed by Kim *et al.* (1999) have Nb/Zr mostly between 0·21 and 0·25, whereas monzonitic lithic fragments (equivalent to our phaneritic lithics) that were analysed by Kim *et al.* (2008) have Nb/Zr up to 0·45. Clearly, different processes fractionated Nb with respect to Zr in the intrusive rocks on Ulleung compared with the extrusive rocks.

For the whole Ulleung suite, light REE (LREE) tend to be depleted with respect to heavy REE (HREE) with increasing Th abundance; that is, La/Yb is negatively correlated with Th abundance (Fig. 8h). In the tephra samples of Stage 4 the REE behaviour is not consistent with the trend defined by samples from the Dodong Basalt, the dykes and the majority of trachyte lavas (Stages 1–3). The pumices have lower REE contents at comparable degree of enrichment (Th concentration) and they lie on a separate trend (Fig. 8b). Additionally, Tephra 5 is extremely enriched in incompatible trace elements (50–60 ppm Th as opposed to a range of 5–30 ppm for the Dodong Basalt, trachytes and Tephras 1–4; Fig. 8). A negative Eu anomaly (Eu/Eu* <1, with Eu/Eu* = chondrite-normalized Eu/[(Sm + Nd)/2]) is present in the chondrite-normalized REE patterns of some of the most evolved samples (trachyte and phonolite) but not all the evolved samples display this type of REE pattern (Figs 8f and 9). The chondrite-normalized REE patterns of Tephra 5, along with trachytic dykes and lava flows from Stage 2, have the most extreme negative Eu anomalies (Eu/Eu* <0·5), whereas Tephra 1–4, Trachyte 3 and some Trachyte 2 samples show only

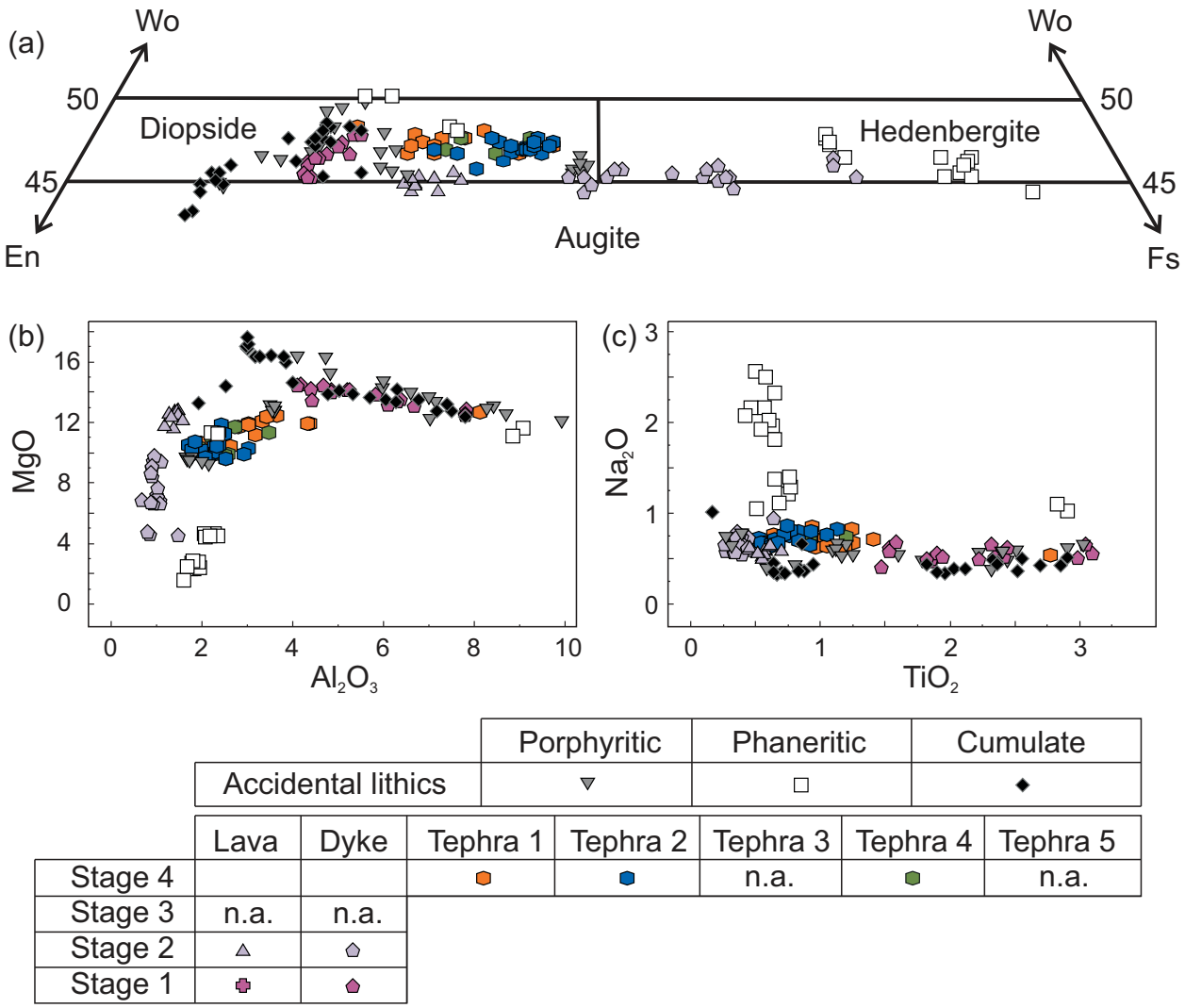

Fig. 4. Chemical classification and characteristics of clinopyroxenes from the Ulleung sample suites. Noteworthy features are the similarity between Stage 1 and mafic cumulates, the grouping of Stage 2 trachytes (b), the similarity between Stage 4 and porphyritic lithic NA05B with relatively higher MgO and TiO_2 and the high-Na pyroxenes from the phaneritic accidental lithic sample [NA11D; (c)]. n.a., not available.

minor depletion in Eu or no anomaly at all. One sample from the phaneritic accidental lithic suite (NA11B) displays a positive Eu anomaly (Eu/Eu* = 1·86).

Chondrite-normalized REE patterns for all analysed samples show some similarities (Fig. 9). LREE are enriched relative to HREE; $(La/Yb)_N$ ratios range from 18·3 to 30·2 in volcanic rocks (Fig. 8h). Comparison of chondrite-normalized REE patterns indicates that the mafic cumulates are the least enriched in REE (Fig. 9b). The phaneritic lithics have characteristic patterns intermediate between those of the mafic cumulates and the trachytes. The REE patterns of Trachyte 2 are similar to those of the Dodong Basalt, but those of Trachyte 3 (along with the porphyritic accidental lithics) show greater depletion in middle REE (MREE) and consequently flatter HREE patterns. This characteristic is further accentuated in the tephra samples, which stand out from the other Ulleung suites by their concave-upward HREE patterns, with HREE slightly more enriched compared with MREE, particularly in Tephra 5 (Fig. 9g). Two samples from the phaneritic lithics (NA11D, NA13A) have REE patterns intermediate between Tephra 5 and Tephras 1–4.

On primitive mantle-normalized multi-element diagrams (Fig. 10) the mafic cumulates are the least enriched in incompatible elements and show the most uniform patterns. Samples of the Dodong Basalt have a notable negative K spike. The evolved samples generally show enrichment compared with the Dodong Basalt, apart for negative spikes for Ba, Sr and Ti (Fig. 10). Samples of Tephra 5 show the greatest enrichments of incompatible elements and the greatest relative depletions in Ba, Sr, Eu

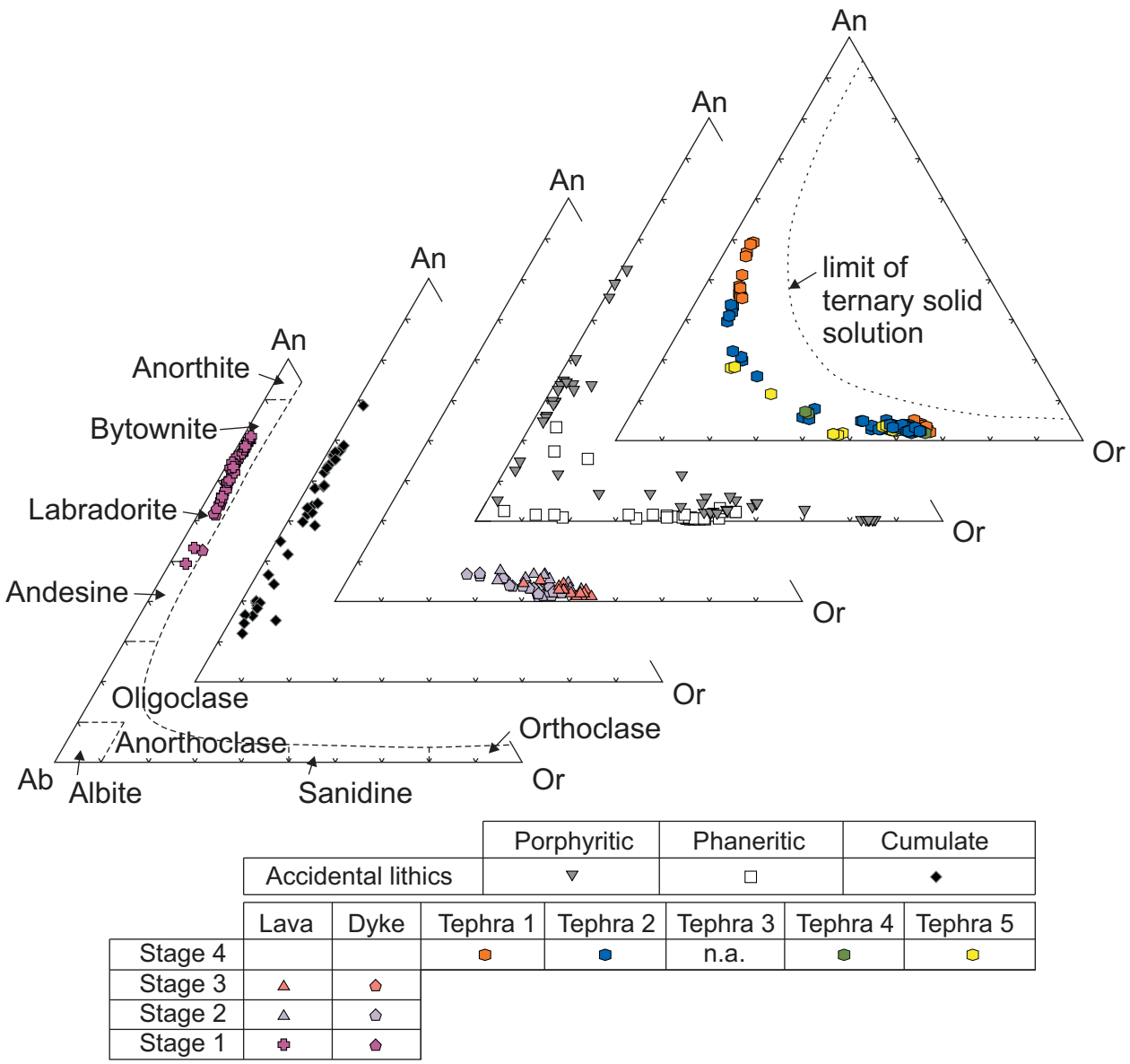

Fig. 5. Compositional variation in Ulleung feldspars, plotted in terms of relative proportions of An (anorthite), Ab (albite) and Or (orthoclase) components. No data for feldspars in Tephra 3 are available. n.a., not available.

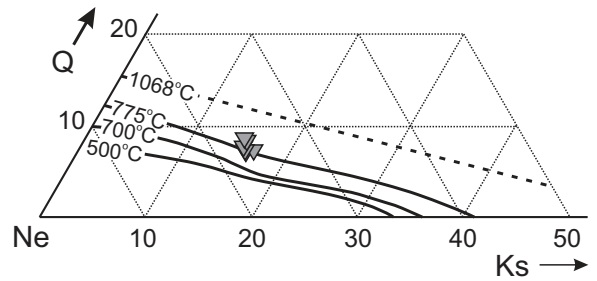

Fig. 6. Nepheline composition (from phaneritic lithic fragment sample NA11C) plotted in the SiO_2–$NaAlSiO_4$–$KAlSiO_4$ (Q–Ne–Ks, Quartz–Nepheline–Kalsilite) system; isotherms are from Hamilton (1961).

and Ti (Fig. 10g). Tephra 5 samples also show a relative negative K anomaly as opposed to Tephras 1–4, which do not have a K anomaly (Fig. 10g and h). Tephras 1–4 show depletion of Sm, Dy and Y relative to the Dodong Basalt. Phaneritic lithic samples represent magmas at different stages of chemical evolution (Fig. 8) and hence have the largest heterogeneity within the group (Fig. 10f).

Sr, Nd and Pb isotopes

Investigations of the isotopic characteristics of the mantle beneath the Korean region have been presented by Choi *et al.* (2005, 2006). Those researchers concluded that melts represented by eruptive products such as those of

Table 7: Major element composition of representative samples from Ulleung Island

Sample:	UL02	UL-14	UL-25	UL-27	UL08b	UL-12	UL38	UL-18	NA-11e	NA-05a
Stage:	1	1	1	1	2	2	2	3	CM	PO
SiO_2	50·94	52·26	51·65	49·04	63·37	63·31	61·29	59·89	45·53	55·03
TiO_2	2·91	2·73	3·22	3·02	0·31	0·47	0·60	0·62	2·32	1·59
Al_2O_3	18·15	19·13	19·94	17·64	18·45	18·55	18·68	19·67	9·88	18·36
FeO_t	8·76	8·20	6·89	9·71	4·08	3·44	3·90	3·44	11·71	6·69
MnO	0·21	0·14	0·11	0·16	0·18	0·22	0·17	0·14	0·17	0·16
MgO	2·76	2·36	2·39	4·48	0·21	0·39	0·67	0·52	14·81	2·64
CaO	8·02	6·84	8·46	8·22	0·97	1·11	1·50	2·17	12·03	4·50
Na_2O	3·89	5·40	4·93	4·21	6·56	6·25	6·43	6·45	1·70	5·45
K_2O	3·46	1·93	1·29	2·60	5·81	6·19	6·59	6·94	1·59	5·18
P_2O_5	0·89	1·01	1·12	0·92	0·06	0·08	0·18	0·15	0·27	0·40
Total	100·00	100·00	100·00	100·00	100·00	100·00	100·00	100·00	100·00	100·00
H_2O	0·99	1·34	1·06	1·00	0·71	1·02	0·16	0·04	0·10	0·07
LOI	2·16	2·32	2·24	1·19	1·47	1·27	0·07	−0·09	0·69	0·11
CIPW norm (anhydrous with $Fe^{3+}/Fe^{2+}=0·2$)										
Plagioclase	49·92	65·12	70·12	47·61	58·62	56·96	45·65	38·83	18·51	39·83
Orthoclase	20·45	11·41	7·56	15·31	34·28	36·52	38·89	41·01	9·40	30·55
Nepheline	2·55	1·47		5·14	0·34	0·09	6·14	10·78	5·64	8·99
Diopside	10·08	4·28	5·02	10·82	0·60	0·57	3·09	4·76	34·66	7·80
Hypersthene			3·54							
Olivine	7·28	8·21	3·36	10·88	4·44	3·93	3·72	2·23	23·91	7·25
Acmite										
Na_2SiO_3										
Ilmenite	5·51	5·18	6·10	5·74	0·59	0·89	1·14	1·18	4·39	3·00
Magnetite	2·15	2·02	1·70	2·38	1·00	0·84	0·96	0·84	2·87	1·64
Apatite	2·06	2·32	2·59	2·13	0·14	0·19	0·42	0·35	0·63	0·93
Total	100·00	100·01	99·99	100·01	100·01	99·99	100·01	99·98	100·01	99·99
Mol. $Al_2O_3/(Na_2O+K_2O)$	1·79	1·74	2·10	1·81	1·08	1·09	1·06	1·09	2·19	1·26
Mol. $Al_2O_3/(CaO+Na_2O+K_2O)$	0·73	0·82	0·80	0·71	0·98	0·98	0·91	0·89	0·37	0·81

Sample:	NA-11a	NA-11b	NA-11c	NA-11d	NA-11h	NA-05e	UL12/8	UL12/16	UL12/17	Unit#6C
Stage:	PH	PH	PH	PH	PH	4 Tephra 2	4 Tephra 2	4 Tephra 2	4 Tephra 2	4 Tephra 5
SiO_2	54·82	62·29	61·62	61·90	42·80	60·42	60·23	60·69	60·88	59·64
TiO_2	1·61	0·66	0·37	0·38	4·21	0·61	0·65	0·53	0·52	0·15
Al_2O_3	18·64	19·12	18·58	19·42	15·41	19·44	19·51	19·47	19·48	20·64
FeO_t	6·37	2·66	4·24	2·50	13·93	3·39	3·50	3·26	3·20	2·96
MnO	0·16	0·09	0·19	0·16	0·18	0·14	0·14	0·15	0·14	0·24
MgO	2·23	0·62	0·46	0·13	5·90	0·46	0·52	0·35	0·36	0·03
CaO	4·72	1·43	1·55	1·24	12·06	1·76	1·88	1·59	1·57	0·98
Na_2O	5·73	6·12	6·88	7·54	2·83	6·52	6·26	6·92	6·68	9·63
K_2O	5·16	6·87	6·02	6·68	2·19	7·14	7·20	6·95	7·07	5·71
P_2O_5	0·57	0·13	0·09	0·05	0·48	0·12	0·11	0·09	0·09	0·02
Total	100·00	100·00	100·00	100·00	100·00	100·00	100·00	100·00	100·00	100·00
H_2O	0·11	0·12	0·13	0·05	0·17	0·06	0·26	0·16	0·11	0·32
LOI	0·23	0·27	0·06	0·08	2·80	0·51	1·37	1·67	0·97	1·16

(continued)

Table 7: Continued

Sample:	NA-11a	NA-11b	NA-11c	NA-11d	NA-11h	NA-05e	UL12/8	UL12/16	UL12/17	Unit#6C
Stage:	PH	PH	PH	PH	PH	4 Tephra 2	4 Tephra 2	4 Tephra 2	4 Tephra 2	4 Tephra 5
CIPW norm (anhydrous with $Fe^{3+}/Fe^{2+}=0{\cdot}2$)										
Plagioclase	39·04	49·24	47·99	40·69	24·45	38·38	38·75	38·66	39·68	36·45
Orthoclase	30·43	40·54	35·52	39·48	12·88	42·14	42·55	41·01	41·72	33·74
Nepheline	10·44	3·77	6·64	11·89	12·06	10·53	9·77	11·59	10·37	20·52
Diopside	8·09	1·51	4·40	5·12	27·78	4·49	4·05	4·95	4·25	4·21
Hypersthene										
Olivine	6·05	2·72	3·50	0·87	10·32	2·18	2·54	1·76	1·99	2·04
Acmite				1·02						1·45
Na_2SiO_3						0·00				1·27
Ilmenite	3·04	1·25	0·70	0·72	7·98	1·16	1·23	1·01	0·99	0·28
Magnetite	1·57	0·65	1·04	0·10	3·42	0·84	0·86	0·80	0·78	
Apatite	1·32	0·30	0·21	0·12	1·11	0·28	0·25	0·21	0·21	0·05
Total	99·98	99·98	100·00	100·01	100·00	100·00	100·00	99·99	99·99	100·01
Mol. $Al_2O_3/(Na_2O+K_2O)$	1·24	1·09	1·04	0·99	2·19	1·05	1·08	1·03	1·04	0·94
Mol. $Al_2O_3/(CaO+Na_2O+K_2O)$	0·79	0·95	0·90	0·89	0·53	0·90	0·91	0·89	0·91	0·87

Ulleung Island have an ultimate origin in the shallow asthenosphere and have ocean island basalt (OIB)-like characteristics reflecting mixtures of depleted mid-ocean ridge basalt (MORB) mantle (DMM), and enriched mantle I (EMI), with a lesser contribution of EMII (Choi *et al.*, 2006). Few of the samples collected in this study show characteristics of primary, unmodified mantle melts; hence further contributions to knowledge cannot be made with regard to mantle source regions.

The analysed samples have $^{87}Sr/^{86}Sr$ initial ratios ranging from ~0·70449 to ~0·70522 and these are negatively correlated with $^{143}Nd/^{144}Nd$, which varies from ~0·51254 to ~0·51263 (Fig. 11). These new results overlap with the Sr and Nd isotope data presented by Kim *et al.* (1999), although the latter included samples with very high $^{87}Sr/^{86}Sr$, which they attributed to seawater contamination (Fig. 11b); these contaminated samples are not considered in the following descriptions and interpretations. The new data reinforce the distinction identified by Kim *et al.* (1999) between the Dodong Basalt and older trachyte units (Stages 1 and 2) and younger trachytes and tephras (Stages 3 and 4, Fig. 11b). Noteworthy is the wide variability in the isotopic compositions of Stage 3 trachytes, which overlap with those of both Stage 1+2, and Stage 4 (Fig. 11b). The phaneritic lithic fragments, dated by Kim *et al.* (2008) as younger than 300 ka, have isotopic characteristics akin to Stages 3 and 4 units. They are therefore grouped with the latter in the Th vs $^{87}Sr/^{86}Sr$ plot shown in Fig. 11e. It is apparent from this figure that Stage 4 (including some Stage 3 samples) units show less variation in $^{87}Sr/^{86}Sr$ ratio as a function of Th abundance compared with Stage 1 and 2 units, although not enough data are available to establish a clear assimilation–fractional crystallization (AFC) trend.

Lead isotope composition varies from ~17·99 to ~18·10 for $^{206}Pb/^{204}Pb$, from ~15·51 to ~15·54 for $^{207}Pb/^{204}Pb$ and from ~38·78 to ~38·89 for $^{208}Pb/^{204}Pb$. The same distinction between Stage 1+2 and Stage 3+4 units as observed in $^{87}Sr/^{86}Sr$ and $^{143}Nd/^{144}Nd$ is also seen in Pb isotopes. Stage 3+4 units have lower $^{208}Pb/^{204}Pb$ at similar $^{206}Pb/^{204}Pb$ compared with Stage 1+2 units (Fig. 11f).

DISCUSSION

This study is based on a sample set from the emergent portion of Ulleung volcano and, given that the island lies in 2000 m of water, it does not represent the entire volcanic history. Kim *et al.* (1999, 2008) presented a generalized model to explain the chemical evolution of eruptive products exposed on Ulleung Island and their relationship with intrusive rocks erupted as accidental lithic inclusions. The present study investigates pre-eruptive conditions and their control on the eruption styles of the evolved magmas. In particular, trachytes of Stages 2 and 3 mainly erupted effusively, whereas the phonolites of Stage 4 erupted explosively. To this end we use the suite of lithic fragments included in the caldera eruptive deposits to gain a further insight into pre-eruptive magmatic processes in the sub-volcanic crust.

Significance of the lithic fragment suite

The suite of lithic fragments brought to the surface by the Stage 4 phonolitic explosive eruptions provides a valuable

Table 8: Trace element compositions of representative Ulleung samples

Sample:	UL02	UL-14	UL-25	UL-27	UL08b	UL-12	UL38
Stage:	1	1	1	1	2	2	2
Cs	0·82	1·19	6·40	0·58	1·37	1·57	0·78
Ba	1035·00	1212·46	1491·60	1142·90	31·00	38·61	183·00
Rb	83·00	79·77	106·05	108·12	178·00	146·35	117·00
Sr	990·00	1041·16	1309·97	1023·97	14·00	33·46	97·00
Pb	14·31	9·00	7·00	6·00	24·51	16·00	12·47
Th	11·66	12·35	11·28	8·36	29·33	22·00	13·19
U	1·48	2·37	1·95	1·49	4·92	3·56	2·60
Zr	384·00	377·56	366·02	295·11	1017·00	656·80	499·00
Nb	97·29	110·41	108·20	81·36	240·57	191·24	131·34
Hf	8·21	8·17	8·00	6·54	20·28	15·10	8·90
Ta	6·24	6·82	6·70	4·96	14·84	11·38	7·63
Y	31·06	29·84	30·14	24·09	52·59	41·87	25·55
Sc	12·38	12·17	11·31	15·23	7·89	7·93	6·32
V	155·00	143·57	186·51	214·37	6·00	10·86	7·00
Cr	0·00	5·87	5·90	50·77	4·00	10·05	3·00
Co	27·90	19·62	22·65	33·34	29·20	15·32	11·10
Ni	6·00	6·31	12·07	35·54	0·00	6·03	3·00
Cu	17·00	9·58	6·20	21·79	2·00	10·80	6·00
Zn	105·00	103·36	134·47	92·49	108·00	143·45	90·00
Ga	22·66	25·00	25·50	22·21	35·10	31·88	23·78
La	81·73	86·60	86·65	72·03	158·54	123·49	83·35
Ce	143·68	154·85	163·94	133·59	279·54	234·83	152·18
Pr	15·95	16·68	18·00	14·54	28·93	23·27	14·62
Nd	61·83	62·24	68·61	55·32	97·42	79·45	52·19
Sm	10·99	10·78	11·76	9·68	15·63	12·55	8·19
Eu	3·47	3·37	3·78	3·19	0·34	0·56	1·70
Gd	9·09	8·90	9·50	7·68	12·41	10·37	6·30
Tb	1·23	1·16	1·23	0·96	1·85	1·46	0·87
Dy	6·85	6·39	6·93	5·46	11·08	8·63	5·35
Ho	1·23	1·17	1·18	0·98	2·11	1·64	0·98
Er	3·34	3·08	3·08	2·60	6·07	4·71	2·74
Tm	0·43	0·42	0·42	0·35	0·85	0·66	0·40
Yb	2·56	2·43	2·49	2·08	5·44	4·27	2·54
Lu	0·37	0·34	0·34	0·28	0·80	0·61	0·35
Eu/Eu*	1·03	1·02	1·06	1·09	0·07	0·14	0·70
Ce/Ce*	0·92	0·94	0·97	0·96	0·94	1·00	0·98

(continued)

Table 8: Continued

Sample:	UL-18	NA-11e	NA-05a	NA-11a	NA-11b	NA-11c	NA-11d
Stage:	3	CM	PO	PH	PH	PH	PH
Cs	1·48	0·59	0·81	1·26	0·68	0·75	1·04
Ba	653·73	404·21	595·57	1022·28	165·45	21·81	3·65
Rb	155·80	36·94	99·48	108·20	91·54	126·38	193·31
Sr	338·31	447·82	474·40	688·26	70·86	22·77	4·42
Pb	13·00	6·00	9·00	12·00	10·00	8·00	10·00
Th	19·50	4·53	13·38	10·72	6·72	14·17	29·18
U	3·80	0·83	2·70	2·24	1·35	2·71	4·00
Zr	487·77	169·03	379·20	295·07	200·51	484·75	565·04
Nb	136·83	36·76	123·06	119·01	58·48	236·98	275·33
Hf	9·85	4·54	7·81	6·33	4·31	11·41	12·53
Ta	8·02	2·43	6·76	7·37	3·72	10·94	20·98
Y	19·57	16·77	21·93	23·14	12·34	33·25	27·72
Sc	2·78	48·44	10·78	6·88	4·14	6·62	1·85
V	18·04	258·30	100·55	75·68	9·27	8·38	7·76
Cr	4·74	725·14	61·26	22·01	4·42	5·06	5·08
Co	13·42	70·51	31·78	24·87	10·30	15·56	14·92
Ni	5·00	250·18	33·51	16·67	4·90	4·21	4·82
Cu	3·81	36·01	25·69	7·14	3·83	3·77	5·08
Zn	72·09	70·88	96·55	78·18	46·33	80·36	62·54
Ga	21·85	14·38	22·72	20·96	18·08	24·56	24·19
La	86·31	31·05	76·45	82·67	43·84	106·91	127·29
Ce	136·90	57·62	133·67	147·22	72·81	215·27	217·97
Pr	12·51	6·81	13·30	15·45	7·24	23·15	20·51
Nd	40·42	27·67	45·69	54·90	24·91	83·30	64·54
Sm	5·84	5·66	7·41	9·03	4·29	13·53	9·38
Eu	1·95	1·78	2·03	2·79	2·40	0·69	0·70
Gd	4·54	5·05	5·85	6·93	3·34	10·32	7·14
Tb	0·62	0·67	0·81	0·90	0·45	1·37	0·94
Dy	3·88	3·88	4·64	5·12	2·49	7·78	5·77
Ho	0·74	0·68	0·85	0·92	0·49	1·41	1·06
Er	2·21	1·79	2·40	2·48	1·38	3·67	3·12
Tm	0·34	0·24	0·33	0·34	0·19	0·49	0·49
Yb	2·24	1·35	2·10	2·04	1·19	3·11	3·15
Lu	0·34	0·18	0·32	0·29	0·17	0·48	0·47
Eu/Eu*	1·11	1·00	0·91	1·04	1·86	0·17	0·25
Ce/Ce*	0·90	0·93	0·94	0·94	0·91	1·01	0·95

(continued)

Table 8: Continued

Sample:	NA-11h	NA-05e	UL12/8	UL12/16	UL12/17	Unit#6C
Stage:	PH	4 Tephra 2	4 Tephra 2	4 Tephra 2	4 Tephra 2	4 Tephra 5
Cs	1·24	1·41	1·31	1·59	1·54	3·82
Ba	462·40	249·55	361·00	183·57	164·21	12·81
Rb	71·90	144·98	155·42	171·79	170·14	310·32
Sr	733·25	150·52	216·40	108·96	109·80	1·97
Pb	6·00	11·00	15·00	78·18	71·17	53·65
Th	5·73	19·93	20·53	13·00	13·00	24·00
U	0·99	4·14	3·77	4·64	4·40	10·88
Zr	217·97	502·89	554·78	660·65	624·18	1443·24
Nb	55·35	141·50	146·41	178·49	168·69	335·82
Hf	5·65	10·12	10·84	13·25	12·70	26·98
Ta	3·53	8·82	8·77	10·52	9·95	20·29
Y	21·29	19·44	20·23	24·28	23·21	43·65
Sc	32·11	3·23	4·31	3·67	3·73	3·63
V	386·28	14·98	13·77	5·89	6·92	1·97
Cr	249·47	5·21	3·93	7·85	5·94	6·90
Co	48·09	24·22	24·30	18·10	9·40	10·70
Ni	65·79	6·09	0·00	0·00	0·00	0·00
Cu	24·85	8·82	56·07	19·63	13·85	12·81
Zn	109·01	64·95	69·84	70·68	69·24	125·11
Ga	22·67	22·31	22·00	23·24	22·87	34·92
La	44·72	83·33	83·85	98·89	95·29	179·72
Ce	81·35	138·49	136·88	156·31	149·72	270·22
Pr	9·40	12·60	12·08	14·29	13·66	21·69
Nd	37·17	40·20	40·59	46·96	45·37	63·86
Sm	7·21	5·95	6·14	7·13	6·95	8·92
Eu	2·38	1·75	1·88	1·56	1·60	0·26
Gd	6·50	4·56	4·59	5·35	5·08	6·89
Tb	0·87	0·66	0·65	0·76	0·75	1·10
Dy	4·90	3·91	3·96	4·62	4·53	7·28
Ho	0·84	0·74	0·76	0·90	0·88	1·48
Er	2·28	2·18	2·26	2·71	2·55	4·59
Tm	0·30	0·32	0·33	0·41	0·39	0·76
Yb	1·78	2·19	2·29	2·83	2·68	5·42
Lu	0·24	0·34	0·34	0·43	0·39	0·80
Eu/Eu*	1·04	0·99	1·04	0·74	0·79	0·10
Ce/Ce*	0·92	0·93	0·93	0·90	0·90	0·90

Table 9: Isotope data for Ulleung Island rocks

Sample	$^{87}Sr/^{86}Sr$	±2σ	$^{143}Nd/^{144}Nd$	±2σ	$^{206}Pb/^{204}Pb$	$^{207}Pb/^{204}Pb$	$^{208}Pb/^{204}Pb$
NA-05A	0·704526	18	0·512583	7	18·030	15·521	38·792
					18·031	15·522	38·794
NA-05E	0·704489	14	0·512615	7	18·034	15·520	38·782
	0·704449	16	0·512605	8			
NA-11A	0·704494	18	0·512594	8	18·028	15·520	38·785
NA-11D	0·704708	19	0·512592	8	18·070	15·524	38·807
NA-11E	0·704691	17	0·512566	8	18·053	15·521	38·829
	0·704663	17	0·512536	7	18·055	15·523	38·835
UL-18	0·704534	14	0·512631	9	18·056	15·524	38·800
UL-19	0·704843	16	0·512570	7	18·046	15·520	38·846
UL-22	0·704788	18	0·512554	8	17·993	15·521	38·794
UL-25	0·705000	16	0·512558	9	18·039	15·515	38·819
UL-27	0·705220	17	0·512551	7	18·103	15·541	38·891
UL-28	0·704934	20	0·512559	6	17·995	15·519	38·794
Standards							
BCR2	0·704991	13					
BHVO2	0·703432	16					
EN-1	0·709140	15					
JNd-1			0·512099	5			
JNd-1			0·512139	8			
JNd-1			0·512126	8			
BH gal					16·003	15·387	35·659
SRM981					16·934	15·485	36·689
SRM982					16·933	15·483	36·684
SRM983					16·933	15·484	36·685

$^{87}Sr/^{86}Sr$ normalized to $^{88}Sr/^{86}Sr = 8{\cdot}37521$ and reported relative to SRM987 = 0·710230; external precision (2σ) is ≤0·000040. $^{143}Nd/^{144}Nd$ normalized to $^{146}Nd/^{145}Nd = 2{\cdot}0719425$ (equivalent to $^{146}Nd/^{144}Nd = 0{\cdot}7219$) and reported relative to La Jolla = 0·511860; external precision (2σ) is ≤0·000020. Pb mass bias corrected using thallium doping. Fifteen runs of SRM981 (not used to construct the Tl–Pb mass bias correlations) average 16·936 ± 0·005, 15·489 ± 0·009 and 36·701 ± 0·024, consistent with the nominal composition adopted for this standard by Woodhead (2002).

perspective on the nature of the sub-volcanic magmatic system at Ulleung Island. It is important to understand the provenance of these lithic fragments and the genetic links they might have with the extrusive rocks. Kim *et al.* (2008) related the coarse-grained or intrusive rocks (their monzonites) to the extrusive rocks in which they are hosted. In their model these monzonites are the remnants of an open-system magma chamber in which a primitive basaltic magma evolved to form the trachytic extrusive rocks. The presence of mafic cumulates in our sample suite provides further evidence supporting this interpretation. The presence of lithic fragments within the explosive deposits of Stage 4 does not, however, in itself demonstrate a direct genetic link between the two. Nevertheless, radiometric dating of intrusive fragments within the extrusive products at Ulleung carried out by Kim *et al.* (2008) revealed relatively young ages between *c.* 100 and 300 ka. This, as pointed out by Kim *et al.* (2008), overlaps with Stage 3, and given the lifespan of subvolcanic complexes is measured in the hundreds of thousands of years (Allibon

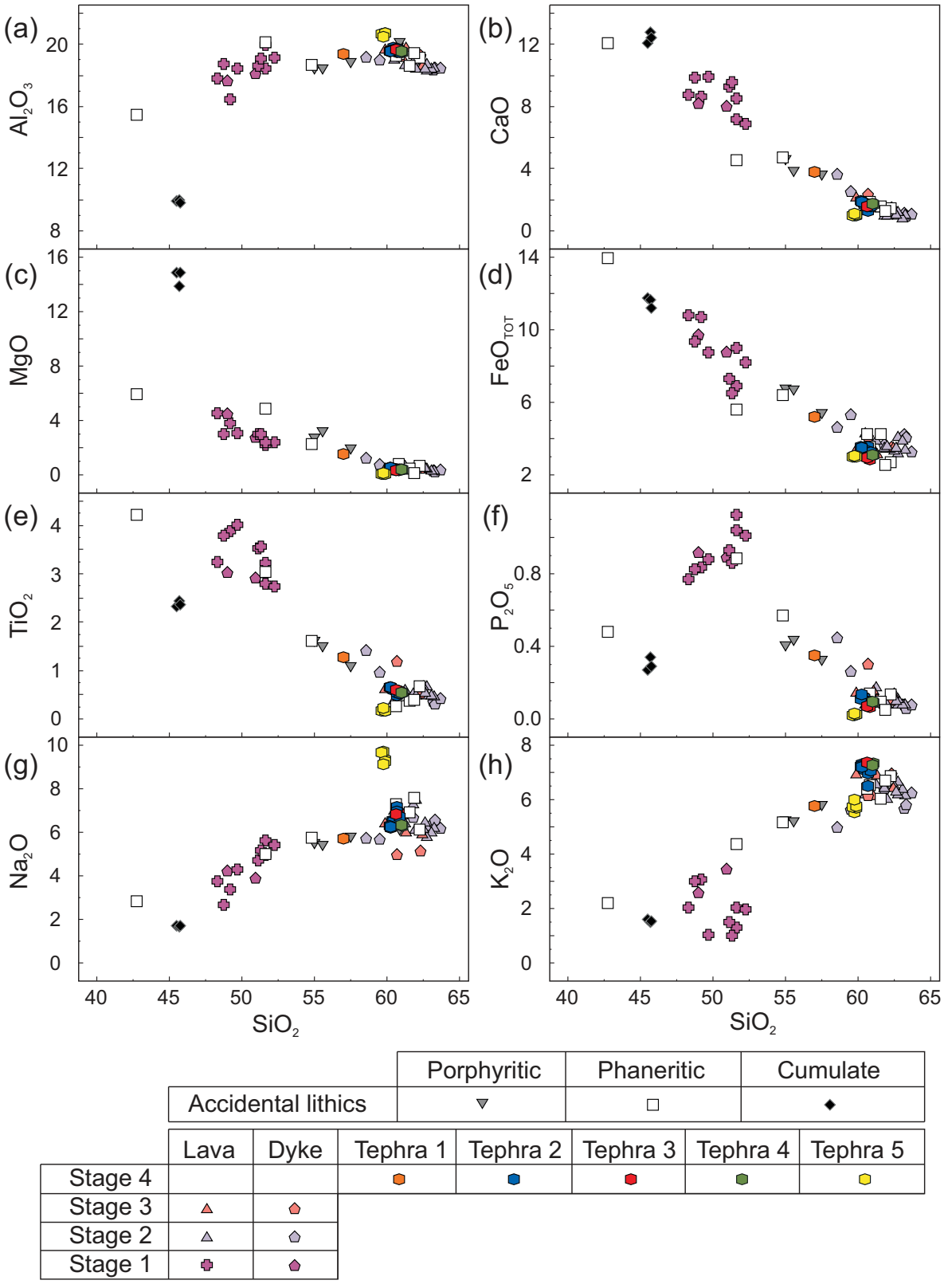

Fig. 7. Major element variations in the Ulleung sample suite.

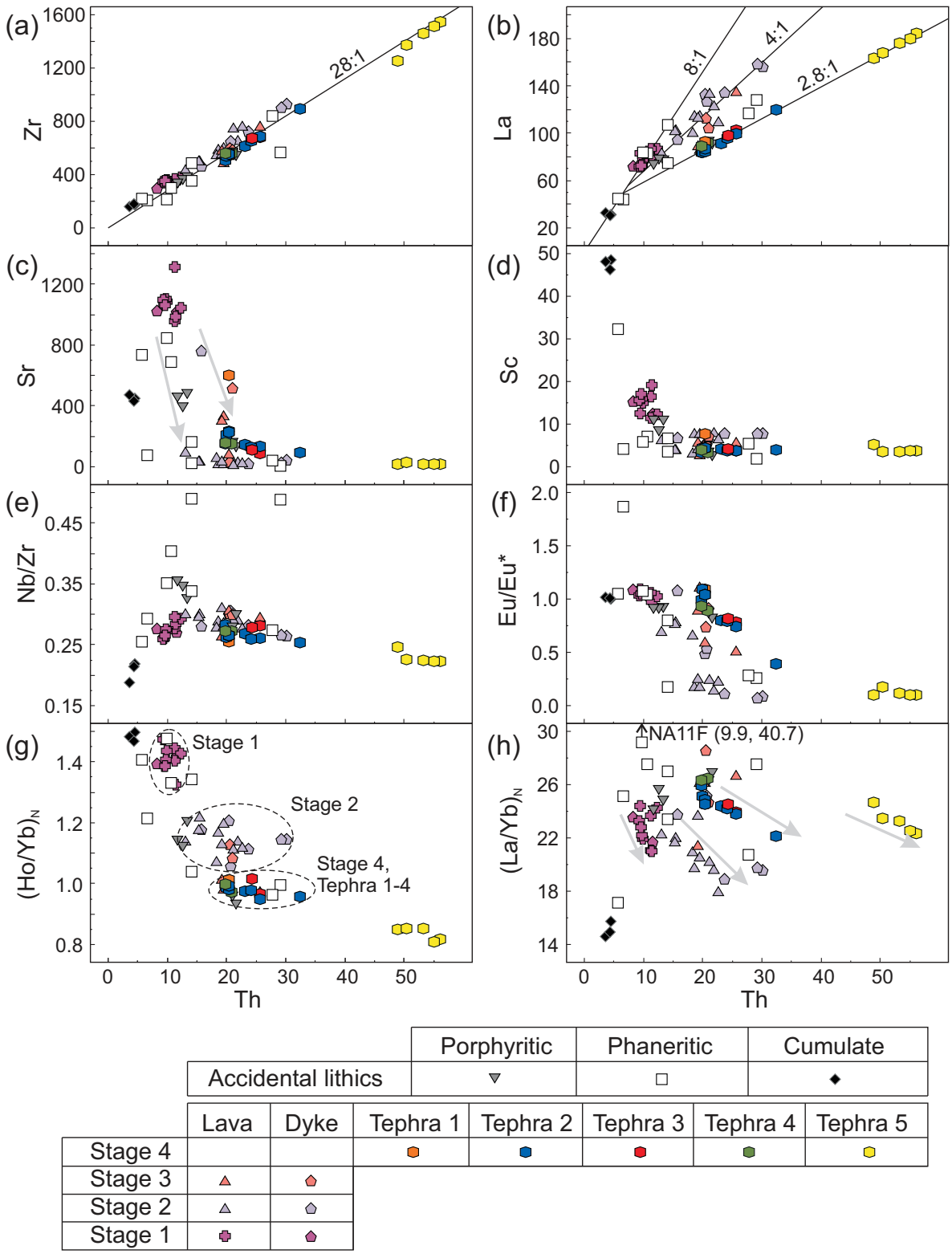

Fig. 8. Trace element variations in the Ulleung sample suite. La, Ho and Yb in (g) and (h) are normalized to chondrite values from Sun & McDonough (1989). Lines in (a) and (b) illustrate constant ratios of the plotted elements for the different sample suites. Grey arrows in (c) indicate possible Sr depletion trends leading to different evolved compositions in trachytes and phonolites. Highlighted areas in (g) illustrate the MREE to HREE relationships between Stage 2 and Stage 4, with Stage 3 and porphyritic accidental lithic samples showing intermediate characteristics between the two. Grey arrows in (h) highlight the sub-parallel negative correlations of the sample groups.

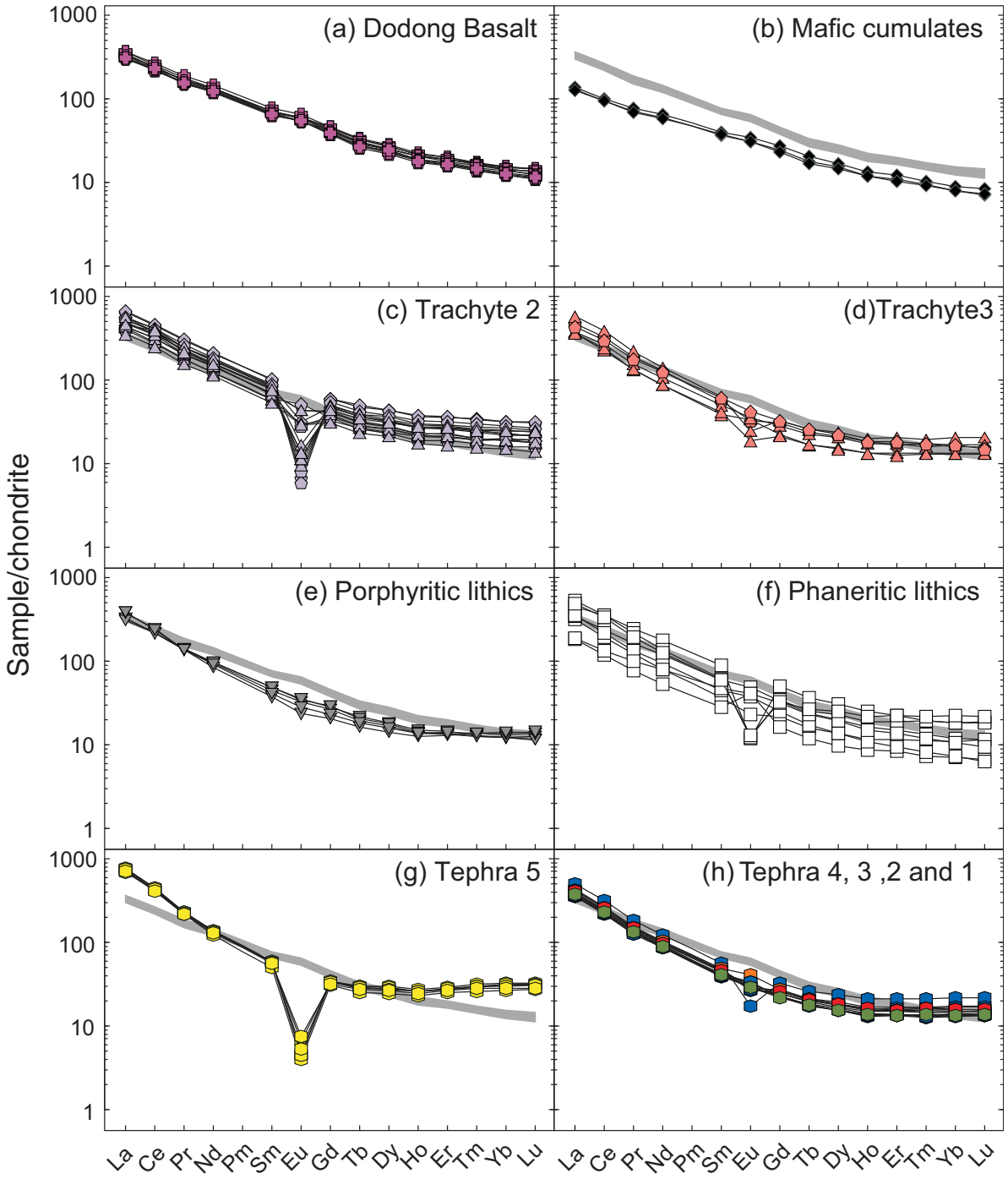

Fig. 9. Chondrite-normalized (Sun & McDonough, 1989) REE patterns. Grey shaded area [diagrams (b)–(h)] is Dodong Basalt. The characteristic flat HREE pattern of Trachyte 3, porphyritic lithics and Tephras 1–4, and the concave-up HREE pattern of Tephra 5, should be noted.

et al., 2011) the lithic clasts may also be related to Stage 4 eruptive products.

The mafic cumulates reported here are not represented in the suite of Kim *et al.* (2008), and therefore an inference as to their possible ages cannot be confidently made. Sample NA11E, representative of the mafic cumulates, has higher $^{87}Sr/^{86}Sr$ and lower $^{143}Nd/^{144}Nd$ compared with Stage 4 and some Stage 3 samples, as well as Pb isotope ratios akin to those of Stage 1 and 2 lavas (Fig. 11e and f). It is therefore unlikely to represent a cumulate from crystallization of the magma that later erupted as Stage 4 phonolite and some Stage 3 trachytes. We therefore

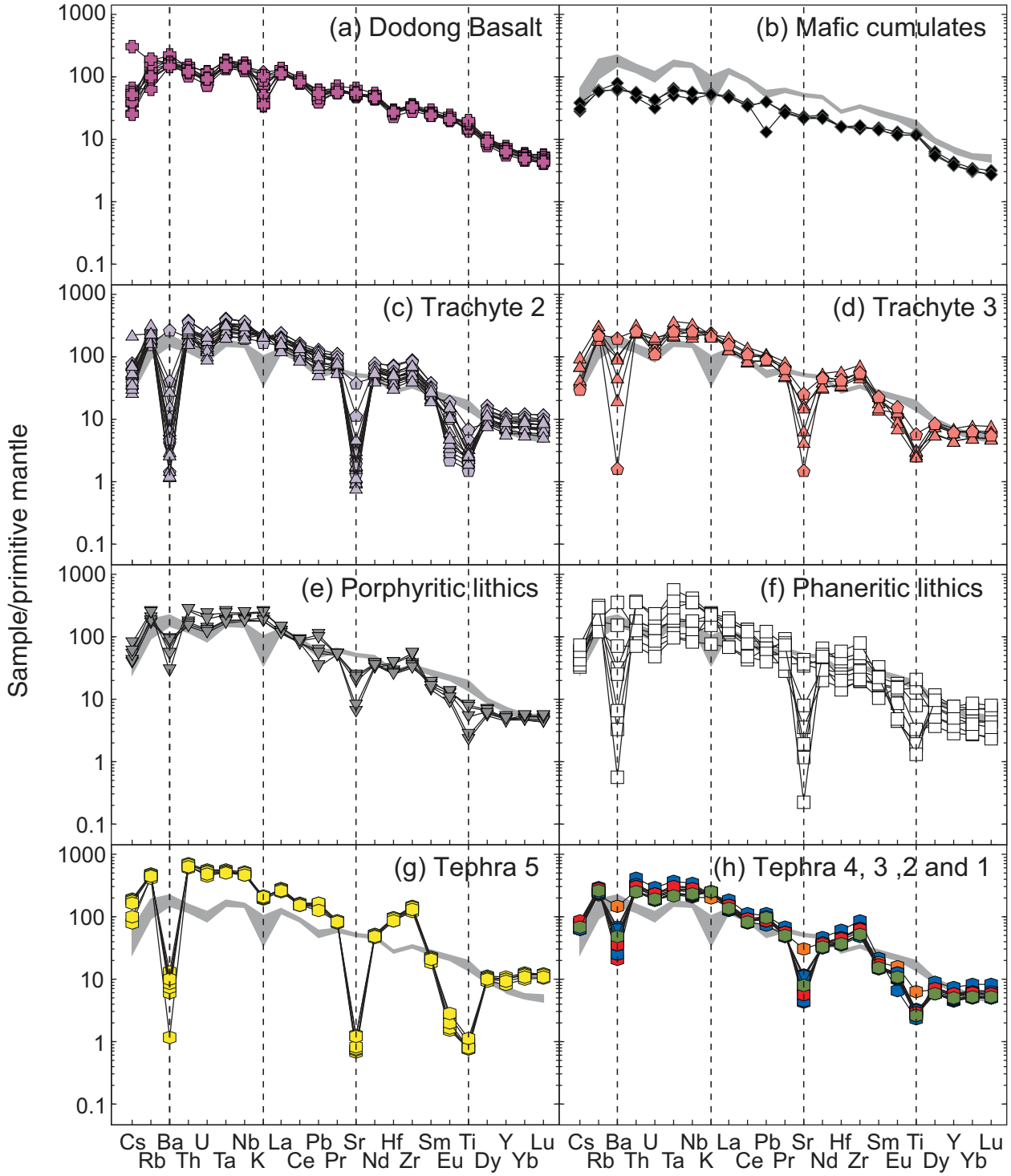

Fig. 10. Primitive mantle-normalized (McDonough & Sun, 1995) multi-element patterns for the Ulleung rock suites. Grey shaded area [(b)–(h)] is Dodong Basalt.

consider the mafic cumulates related to the early magmatic system of Ulleung Island (Stage 1).

Our phaneritic accidental lithic samples span almost the entire compositional spectrum (Fig. 7). However, all but samples NA11A, F and H have $SiO_2 > 60$ wt %, equivalent to the intrusive fragments dated by Kim *et al.* (2008). Of these, sample NA11A (tephriphonolite) has isotopic and trace element compositions related to Stages 3 and 4

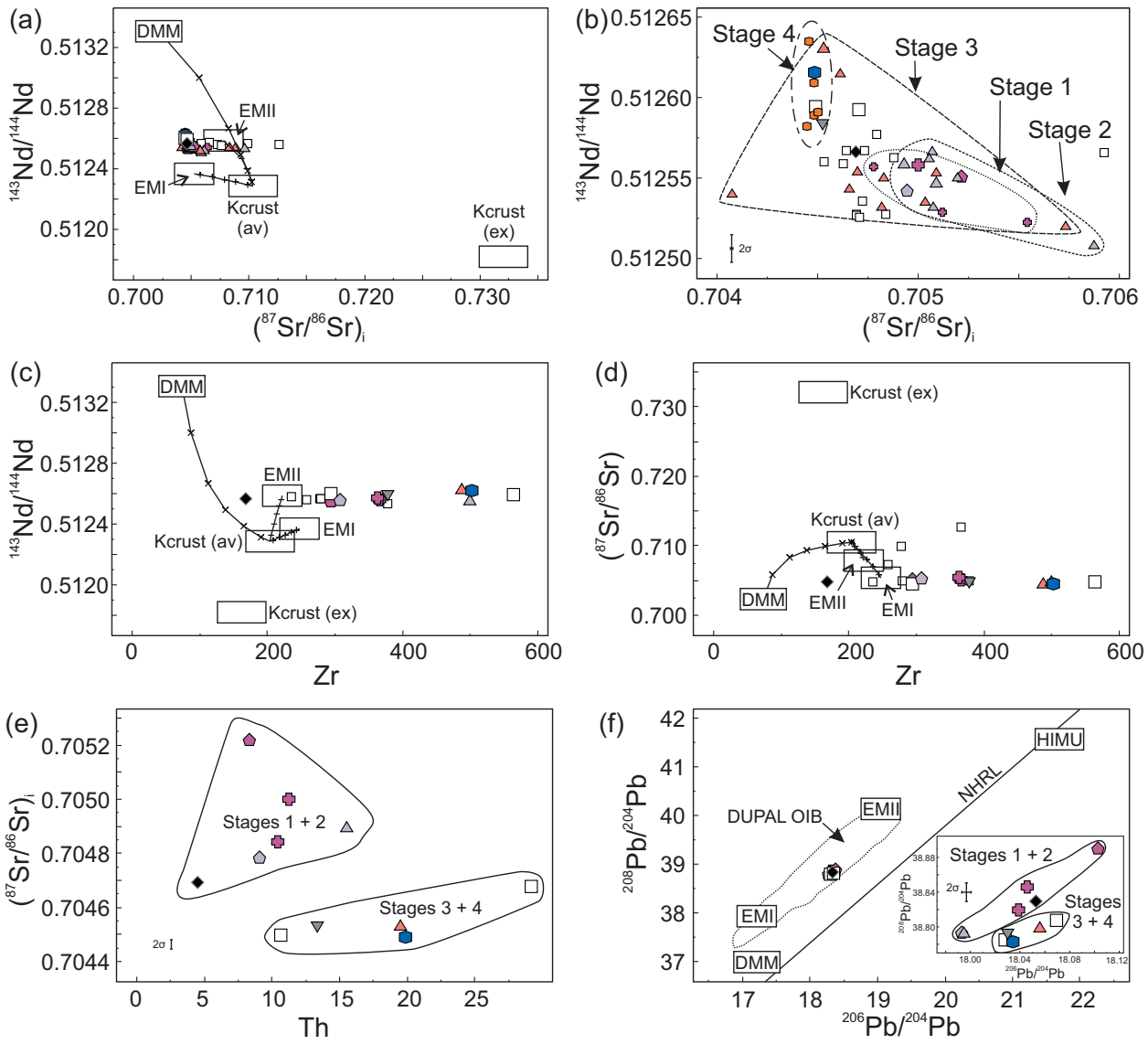

	Porphyritic	Phaneritic	Cumulate
Accidental lithics	▽	□ □K	◆

	Lava	Dyke	Tephra 1	Tephra 2	Tephra 3	Tephra 4	Tephra 5
Stage 4			K		n.a.	n.a.	n.a.
Stage 3	△ △K	n.a.					
Stage 2	△ △K	⬠					
Stage 1	✚ ✚K	⬠					

Fig. 11. Sr–Nd–Pb isotopic variations in the Ulleung samples. Where available, previously published data (small symbols, with superscript K in legend) for intrusive (Kim *et al.*, 2008) and extrusive (Kim *et al.*, 1999) Ulleung Island rocks are shown for comparison. Isotopic compositions of mantle end-members are from Hart *et al.* (1992). Trace element compositions of mantle end-members are from Sun & McDonough (1989) for DMM and from Workman *et al.* (2004) for EMII. For EMI an average value has been used (Weis *et al.*, 1993; Woodhead & Devey, 1993; Barling *et al.*, 1994; Hémond *et al.*, 1994). The fields for average [Kcrust (av)] and extreme [Kcrust (ex)] Korean crust compositions are from Cheong *et al.* (2002) and Williams *et al.* (2009). NHRL is the Northern Hemisphere Reference Line of Hart (1984). The DUPAL OIB isotopic field is after Dupré & Allègre (1983), Hart (1984) and Vidal *et al.* (1984). Model lines in (a), (c) and (d) represent mixing between mantle end-members and average Korean crust at 0·1, 0·3, 0·5, 0·7 and 0·9 fractions. Fields in (e) are drawn to include phaneritic and porphyritic lithics in Stages 3 and 4; these have similar ages (Kim *et al.*, 2008). It should be noted that in (e) only our samples are plotted because the relevant trace element data were not reported by Kim *et al.* (1999).

(Fig. 11e and f) and is therefore also likely to have a relatively young age. A further indication of a relatively young age comes from sample NA11D (phonolite). Despite the fact that it consists almost entirely of a complete network of feldspar crystals, interstices consist of fresh, vesiculated glass. This is good evidence that the lithic clast was cogenetic with the phonolite magma that entrained and erupted it. Additionally, phonolitic tephras contain feldspar glomerocrysts with textures resembling those in the phaneritic intrusive rocks, and may therefore represent entrainment from the walls of the (mushy?) magmatic plumbing system or magma reservoir.

Sample NA11H (compositionally basanite but texturally intrusive) is compositionally similar to the Dodong Basalt (Fig. 7). It is very SiO_2 poor and has incompatible trace element characteristics akin to the mafic cumulates. It is itself, however, unlikely to be a mafic cumulate owing to the relatively low concentrations of MgO, Ni, Cr and Sc and relatively higher abundances of FeO and V compared with the mafic cumulate accidental lithics.

Sample NA11B has the major element characteristics of a trachyte but its incompatible trace elements are not enriched and it is therefore unlikely to represent a residual melt derived from extensive fractional crystallization. The positive Eu anomaly (Figs 8f and 9f) of sample NA11B indicates that it is likely to represent a felsic cumulate. Not all samples in the phaneritic accidental lithic suite can be unambiguously linked to Stage 3+4 magmatism; they nonetheless illustrate a complex magmatic plumbing system with storage, fractionation and accumulation areas dispersed throughout.

The porphyritic accidental lithics are likely to represent near-surface lavas or shallow subvolcanic sill–dyke complexes that were later disrupted and entrained in the explosive eruption deposits of Stage 4. They have major and trace element compositions indicating a lower degree of chemical evolution compared with the sampled trachytic lavas of Stages 2 and 3 (Figs 7 and 8). Their normalized REE pattern (Fig. 9e) have features (concave upwards, lack of Eu anomaly and flat HREE) similar to those of the Stage 3 trachytes (Fig. 9d) or Tephras 1–4 (Fig. 9h). The only samples with 55–58 wt % SiO_2 reported by Kim *et al.* (1999) belong to their post-caldera stage, and they cannot therefore be related to the porphyritic lithics described here. These samples are therefore representative of a magmatic (extrusive) phase transitional between Stage 3 and Stage 4.

Origin of the Stage 4 phonolitic tephras

In this study we are interested in the mechanisms driving the different eruption styles (effusive vs explosive) of the trachytic and phonolitic rocks. Here we analyse and investigate the chemical properties of the two rock suites at Ulleung Island with the additional help of data for the accidental lithic suite. The phonolite tephras of Stage 4 are the youngest eruptive rocks at Ulleung Island (Kim *et al.*, 1999; Im *et al.*, 2012). They have distinct chemical characteristics that differentiate them from trachytic rocks of Stage 2, but have some chemical features in common with some Stage 3 trachytes.

The distinction of the four evolutionary stages of Ulleung is illustrated by the degree of Y or La enrichment (Figs 3d and 8b). Stages 1+2 have steeper slopes of Y and La enrichment compared with Stage 4, with Stage 3 being intermediate. Also, at comparable or larger degrees of Th enrichment, Stage 3+4 units have Sr (100–200 ppm) and Ba (200–400 ppm) abundances that are higher than those observed in the Stage 2 trachytes; Sr and Ba are extremely depleted in the latter group (<100 ppm; Fig. 8c). The weakly concave-upward pattern observed in the normalized REE patterns of the Stage 4 tephra samples is also different from that of Stage 2+3 trachytes (Fig. 9). It may indicate a relatively greater compatibility of MREE in the fractionating solids. Comparatively larger K_D values for MREE in amphibole, clinopyroxene and titanite were determined by Wörner *et al.* (1983) for phonolite of the Laacher See and fractionation of some combination of these phases could therefore explain the development of concave-upward primitive mantle-normalized REE patterns in Ulleung Stage 4 samples. The fractionation of amphibole may also account for the variable Nb/Zr ratio behaviour (Fig. 8e; Francis & Ludden, 1995). Additionally, during electron probe microanalysis a trace mineral phase with up to 30 wt % Nb and Zr oxides was detected in the phaneritic lithic samples. Crystallization + fractionation of this type of phase would certainly have affected the Nb/Zr ratio. Wörner & Schminke (1984) also observed that green Na augite (aegerine–augite) has a greater affinity for Zr and LREE and HREE, whereas brown Ti-augite has a larger K_D for MREE. Sodic pyroxene (Na_2O <2·5 wt %) is present in some Ulleung phaneritic lithic clasts and fractionation of this phase would affect the Zr/Nb ratios.

The Stage 4 phonolites are likely to be consanguineously related to the phaneritic lithic clasts that they contain. As highlighted above, the age of the phaneritic clasts overlaps with the younger phases of magmatism at Ulleung, and they have physical and chemical features suggesting a relationship. Additionally, both rock types contain amphibole, which is absent in the trachytes. The Nb/Zr ratio, which, as explained above, is related to crystallization of sodic pyroxenes and Nb and Zr silicate phases, is relatively high in the phaneritic lithics, whereas it is relatively lower in the Stage 4 phonolites (Fig. 8e). Fractionation of a phase increasing the Nb/Zr ratio in the solid being removed (i.e. the phaneritic portion) will result in a complementary decrease in the Nb/Zr ratio of the residual liquid in equilibrium with it (i.e. the phonolite magma).

Stage 2 trachytic units are isotopically distinct from the Stage 4 phonolitic tephras and two Stage 3 trachyte

samples. Stage 4 and two Stage 3 samples have lower $^{87}Sr/^{86}Sr$ and higher $^{143}Nd/^{144}Nd$ compared with the Stage 1+2 samples (Fig. 11b). Despite its location in the East Sea/Sea of Japan, Ulleung is situated entirely on a stretched continental crust basement (Tamaki *et al.*, 1992; Kim *et al.*, 2011). In our models illustrated in Fig. 11 we have assumed that a potential crustal contaminant of the resident magmas might have a composition similar to Mesozoic intrusive rocks exposed along the eastern coast of the Korean peninsula (Cheong *et al.*, 2002; Williams *et al.*, 2009); these are contiguous with the stretched crustal basement beneath Ulleung. As illustrated by the mixing lines in Fig. 11a, c and d, contamination by crust with an average composition of Korean peninsula Mesozoic intrusive rocks would result in increasing $^{87}Sr/^{86}Sr$ and decreasing $^{143}Nd/^{144}Nd$. The Stage 4 tephra units are therefore unlikely to have been derived by AFC from a parent melt with a composition similar to the Stage 1 Dodong Basalt (the most primitive product from the Ulleung magmatic system). Direct derivation of the Stage 4 phonolites by crustal anatexis is unlikely owing to the generally elevated abundances of Sr and Ba in such melts (Hobson *et al.*, 1998); it should be noted that these elements are present in low abundances in the phonolitic tephras (Figs 8c and 10g, h). Additionally, as modelled, the crustal basement of Ulleung has isotopic characteristics incompatible with such a scenario.

Stage 4 phonolites appear to be unrelated to the parental magmas of Stages 1+2. Their more primitive isotopic characteristics, moreover, raise the possibility that the source magmas for Stage 4 and Stages 1+2 were derived from different domains within a heterogeneous mantle. This is very likely given the characteristics of the mantle beneath Ulleung Island, which has been interpreted to consist of a mixture of DMM + EMI + EMII (Choi *et al.*, 2006). The similarities that some Stage 3 trachyte and porphyritic accidental lithic samples have to the Stage 4 samples, however, suggest that the magmatic system evolved stepwise over time, rather than through a sudden change. Below we investigate and model the parameters of chemical evolution.

Modeling of magmatic evolution

The major and trace element compositions, as well as isotopic and age considerations discussed above, preclude the possibility that the Stage 4 phonolites can be derived from magmas with the compositions of any of the whole-rock samples from the Stage 1 Dodong Basalt. Stage 2 trachytes could nevertheless have been sourced from a magma akin to that erupted during Stage 1. Here we simulate potential fractionation paths and compare these with the observed major and trace element variation.

Crystal fractionation has been modelled using the least-squares mass-balance method of Stormer & Nicholls (1978), employing Microsoft Excel® spreadsheets with mineral data from the selected end-members or compositions between these (Fig. 3b, Tables 1–6). Although these models do not give unique solutions and are based on an assumption that the compositions of the fractionating phases are constant, they allow a semi-quantitative evaluation of the feasibility of fractional crystallization as the process controlling major element chemical variation. We generated Models 1–7 to investigate the chemical variation between and within different stages. The parameters used in each model are reported in Table 10. Assuming simple Rayleigh fractionation, the parameters obtained from the major elements models (e.g. proportions of fractionating phases and fraction of liquid remaining) were used to model trace element behaviour. Distribution coefficients in the different mineral phases were obtained using published data and methods (Nash & Crecraft, 1985; Ewart & Hawkesworth, 1987; Dunn & Sen, 1994; Nielsen *et al.*, 1994; Halliday *et al.*, 1995; Icenhower & London, 1996; Klein *et al.*, 1997; Sano *et al.*, 2002; Tiepolo *et al.*, 2002; Blundy & Wood, 2003; White, 2003; Prowatke & Klemme, 2006).

No whole-rock sample in the analysed suite is sufficiently primitive to approximate a mantle-derived parent melt. All analysed samples have relatively low MgO concentrations and thus Mg-numbers [mol. MgO/(MgO + FeO)], and Ni abundances are <50 ppm (primitive magmas contain 240–390 ppm Ni; Sato, 1977). The magmas represented by the Stage 1 Dodong Basalt must have already undergone considerable fractionation prior to eruption. Model 1 simulates chemical variability within the mafic samples of the Dodong Basalt. Two Stage 1 samples UL27 (trachybasalt) and UL02 (basaltic trachyandesite) were used as parent and daughter respectively. For this pair of compositions the major element variation can be accounted for by removal of *c.* 16% clinopyroxene + olivine + plagioclase + oxide + apatite crystals, with a sum of the residuals squared (SSR) of 0·57. In addition to the major element fit, trace element models are consistent with the observed variation (Table 10, Fig. 12a). This mineral assemblage is consistent with the observed modal proportions of the mafic cumulate accidental lithics, providing further evidence for derivation of these from crystallization of magma that was then extruded to form the Dodong Basalt.

The chemical variation from mafic compositions (Stage 1) to trachyte (Stage 2) is represented in Model 2 (Table 10, Fig. 12b). For this model sample UL02 (basaltic trachyandesite) was taken as the parent and sample UL08b (trachyte) as the daughter. The model predicts removal of *c.* 76% material in various proportions of alkali feldspar, plagioclase, clinopyroxene, oxide and apatite. Although the SSR is very low (0·08), the fit of the trace element model is not ideal. The latter predicts an overenrichment in incompatible elements and a much larger negative Eu anomaly compared with the actual data, and hence the major element model overestimates the amount

Table 10: Results of the mass-balance and fractional crystallization models

	Model 1—UL27 to UL02 (SSR = 0·57)												
Phase:	SiO_2	TiO_2	Al_2O_3	FeO_t	MgO	CaO	Na_2O	K_2O	P_2O_5	Ph %			
Ol	38·98			19·98	40·8	0·23				−4·49			
Cpx	46·14	3·12	7·87	7·74	12·7	21·88	0·56			−1·37			
Pl	52·73		30·2	0·42		12·19	3·85	0·61		−7·41			
Mt		19·08	5·98	68·47	6·47					−2·4			
Ap						56·84			43·16	−0·53		$F = 0·838$	
	Sr	Pb	Th	Zr	Nb	La	Ce	Nd	Sm	Eu	Gd	Dy	Yb
Model 1	1083	13·2	9·7	405	96	79·8	146·8	59·9	10·4	3·4	8·8	6·2	2·4
UL02	990	14·3	11·7	384	97	81·7	143·7	61·8	11·0	3·5	9·1	6·8	2·6
	Model 2—UL02 to UL08b (SSR = 0·08)												
Phase:	SiO_2	TiO_2	Al_2O_3	FeO_t	MgO	CaO	Na_2O	K_2O	P_2O_5	Ph %			
Ksp	66·01		19·28	0·17		0·39	5·61	8·54		−23·72			
Cpx	46·14	3·12	7·87	7·74	12·7	21·88	0·56			−16·3			
Pl	52·73		30·2	0·42		12·19	3·85	0·61		−24·08			
Mt		19·08	5·98	68·47	6·47					−10·78			
Ap						56·84			43·16	−2·02		$F = 0·231$	
	Sr	Pb	Th	Zr	Nb	La	Ce	Nd	Sm	Eu	Gd	Dy	Yb
Model 2	5	32·1	43·4	1488	397	214·3	354·0	134·4	22·9	0·0	26·7	19·7	7·5
UL08b	14	12·4	29·3	1017	241	158·5	279·5	97·4	15·6	0·3	12·4	11·1	5·4
	Model 3—NA05E to UL12/16 (9SSR = 0·07)												
Phase:	SiO_2	TiO_2	Al_2O_3	FeO_t	MgO	CaO	Na_2O	K_2O	P_2O_5	Ph %			
Ksp	65·3		19·21	0·06		0·62	4·36	10·45		−8·36			
Ox		17·29	6·71	69·46	6·54					−0·68			
Ap						56·84			43·16	−0·34		$F = 0·906$	
	Sr	Pb	Th	Zr	Nb	La	Ce	Nd	Sm	Eu	Gd	Dy	Yb
Model 3	52	18·8	21·9	646	156	88·1	145·8	41·9	6·2	1·5	4·9	4·2	2·4
UL12/16	109	67·5	25·7	661	178	98·9	156·3	47·0	7·1	1·6	5·3	4·6	2·8
	Model 4—UL12/8 to UL12/17 (SSR = 0·10)												
Phase:	SiO_2	TiO_2	Al_2O_3	FeO_t	MgO	CaO	Na_2O	K_2O	P_2O_5	Ph %			
Ksp	64·3		20·21	0·13		1·04	4·6	9·72		−11·31			
Amph	40·49	6·19	13·33	11·79	12·34	11·8	2·36	1·7		−2·64			
Mt		20·89	2·61	74·83	1·67					−0·61		$F = 0·854$	

(continued)

Table 10: Continued

	Sr	Pb	Th	Zr	Nb	La	Ce	Nd	Sm	Eu	Gd	Dy	Yb
Model 4	47	17·5	24·0	643	170	97·6	158·9	46·4	6·9	1·6	5·1	4·4	2·6
UL12/17	110	71·2	24·2	624	169	95·3	149·7	45·4	6·9	1·6	5·1	4·5	2·7

Model 5—UL12/17 to Unit#6C (SSR = 0·48)

Phase:	SiO_2	TiO_2	Al_2O_3	FeO_t	MgO	CaO	Na_2O	K_2O	P_2O_5	Ph %			
Amph	40·44	4·51	11·74	21·11	6·71	11·39	2·17	1·93		–5·58			
Ksp	64·3		20·21	0·13		1·04	4·6	9·72		–49·09			
Mt		20·89	2·61	74·83	1·67					–0·56		$F = 0·448$	

	Sr	Pb	Th	Zr	Nb	La	Ce	Nd	Sm	Eu	Gd	Dy	Yb
Model 5	0	157·7	53·0	1350	365	196·9	276·9	66·8	8·1	0·4	6·5	6·2	4·3
Unit#6C	2	53·7	55·2	1443	336	179·7	270·2	63·9	8·9	0·3	6·9	7·3	5·4

Model 6—UL38 to Unit#6C (SSR = 1·11)

Phase:	SiO_2	TiO_2	Al_2O_3	FeO_t	MgO	CaO	Na_2O	K_2O	P_2O_5	Ph %			
Amph	39·4	6·59	14·98	10·17	13·22	12·02	2·12	1·51		–4·26			
Ksp	66·01		19·28	0·17		0·39	5·61	8·54		–64·83			
Ox		19·9	5·66	68·59	5·86					–3·14		$F = 0·278$	

	Sr	Pb	Th	Zr	Nb	La	Ce	Nd	Sm	Eu	Gd	Dy	Yb
Model 6	0	46·2	46·4	1721	451	290·0	528·8	177·2	26·3	0·4	20·1	16·6	8·3
Unit#6C	2	53·7	55·2	1443	336	179·7	270·2	63·9	8·9	0·3	6·9	7·3	5·4

Model 7—UL38 to UL12 (SSR = 1·84)

Phase:	SiO_2	TiO_2	Al_2O_3	FeO_t	MgO	CaO	Na_2O	K_2O	P_2O_5	Ph %			
Ksp	65·63		19·56	0·23		0·69	5·15	8·73		–17·65			
Cpx	52·67	0·46	1·42	10·21	12·88	21·72	0·64			–1·15			
Mt		22	1·84	73·89	2·27					–2·11		$F = 0·791$	

	Sr	Pb	Th	Zr	Nb	La	Ce	Nd	Sm	Eu	Gd	Dy	Yb
Model 7	8	16·7	16·6	625	165	104·8	191·5	65·7	10·3	1·4	7·9	6·7	3·2
UL12	25	25·0	18·1	776	191	123·5	234·8	79·5	12·5	0·6	10·4	8·6	4·3

Mineral compositions recalculated to 100% totals. SSR, sum of the squared residuals for each model; Ph %, phase per cent removed relative to initial melt; *F*, weight fraction of melt remaining after fractionation. Trace element distribution coefficients in the mineral phases were obtained using published data and methods (Nash & Crecraft, 1985; Ewart & Hawkesworth, 1987; Dunn & Sen, 1994; Nielsen *et al.*, 1994; Halliday *et al.*, 1995; Icenhower & London, 1996; Klein *et al.*, 1997; Sano *et al.*, 2002; Tiepolo *et al.*, 2002; Blundy & Wood, 2003; White, 2003; Prowatke & Klemme, 2006). Ol, olivine; Cpx, clinopyroxene; Pl, plagioclase; Amph, amphibole; Mt, magnetite; Ap, apatite.

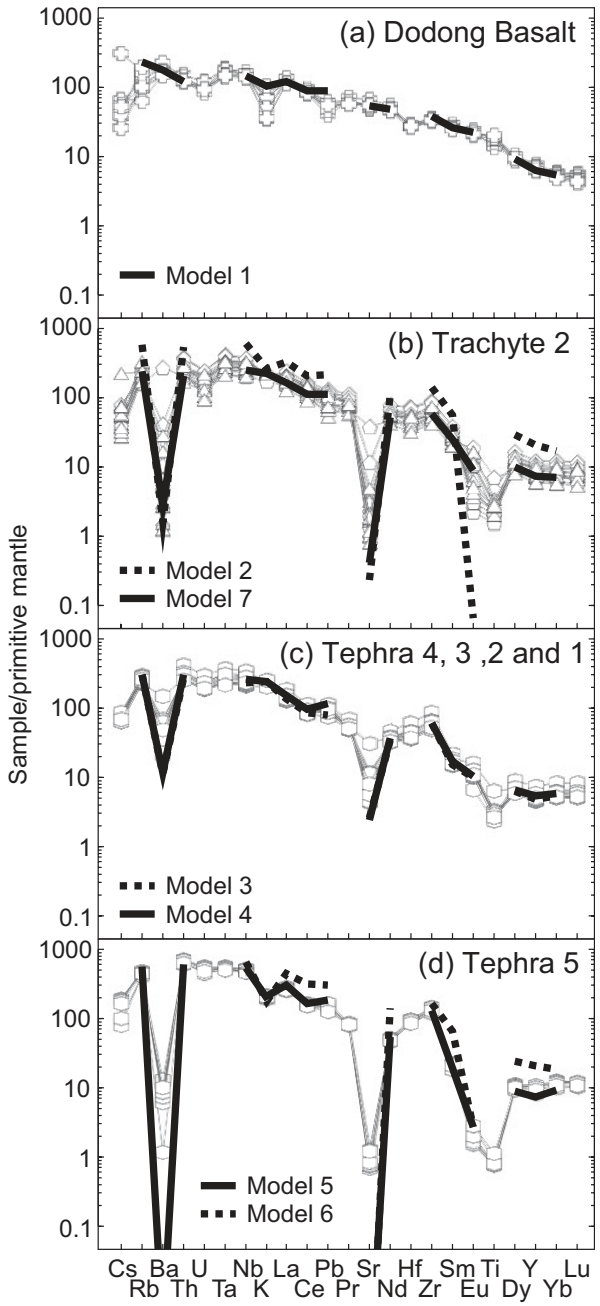

Fig. 12. Results of trace element models, based on the least-squares major element models in Table 10 and described in the text.

of material that needs to be removed. It is possible that inclusion of other mineral phases such as amphibole in the fractionating assemblage may improve the model results (Wilson *et al.*, 1995). Given, however, that this mineral was not observed in either Dodong Basalt or Stage 2 and 3 trachytes, its inclusion in a model does not seem justified and would be speculative only. Stage 4 phonolites as well as the porphyritic lithics do contain amphibole, and their concave-up REE patterns suggest amphibole involvement. However, the absence of any sample with a composition that might represent a mafic parent to this magmatic stage precludes testing of a viable model.

The distribution of data points on the TAS diagram (Fig. 3b) can be used to argue that the compositional spectrum of Stage 4 tephras can only be accounted for in two steps. For step 1 (Models 3 and 4), samples NA05E and UL12-8 (both phonolite) have been used as starting (parental) compositions and sample UL12-16 and UL12-17 (phonolite) as the end (daughter) composition, respectively. These models suggest that between 9 and 15% fractionation of an assemblage including alkali feldspar + apatite ± amphibole ± oxide is necessary to account for the observed variation. These models give relatively low SSR (between 0·07 and 0·1) and the model trace element compositions fit very well with the observed data (Table 10, Fig. 12c).

The second step in the two-step fractionation model involves sample UL12-17 as the parent and sample UNIT#6C (both phonolites) as the daughter (Model 5). This models the evolution of Tephra 5, which was erupted prior to Tephra 2 (represented by sample UL12-17). Despite this inverse temporal relationship, major and trace element variation is consistent with this parent–daughter relationship (Fig. 3). Additionally, these samples are both from a continuous succession of tephras erupted within 15 kyr. Model 5 requires the removal of 55% of mainly K-feldspar with minor amphibole and oxides, with SSR of 0·48. The trace element model shows a good fit with the observed data (Table 10, Fig. 12d). An alternative model for the derivation of the lower tephras from a trachytic sample (UL38) has also been tested (Model 6). This requires the removal of *c.* 72% of mainly alkali feldspar with minor amphibole and oxides, and has a relatively high SSR of 1·11. The trace element model prediction is not as good as in the case of Model 5 (Table 10, Fig. 12d). Comparison of these two models leads to the conclusion that Tephra 5 is more likely to have been derived from magma similar to the coeval phonolitic Stage 4 Tephras 1–4 rather than from a trachyte.

To model the evolution within the trachyte magma of Stage 2 (Model 7; Table 10, Fig. 12b) sample UL38 (trachyte), which was collected from a dome, was used as the parental magma composition. This sample has the most primitive composition amongst the trachytic samples with the lowest Th abundance. Sample UL12 (trachyte) was selected as the daughter composition as it is the most evolved member of the extrusive samples of Stage 2. The results are consistent with a fractionation assemblage dominated by alkali feldspar with various lesser amounts of clinopyroxene and Fe–Ti oxides; the model involves removal of *c.* 21% solid. The SSR is relatively high at 1·84 but the trace element model gives a good fit to the observed data (Fig. 12b).

These models suggest that Tephra 5 is unusual. Variability within the Stage 2 trachytes and within Tephras 2–4 (Stage 4) can be accounted for by removal of <25 vol. %, whereas to go from Tephra 2–4 to Tephra 5 >50 vol. % removal is required. This explains the relatively high abundances of incompatible trace elements in Tephra 5 (Figs 8–10).

Temperature and pressure constraints on magmatic evolution

Amphibole compositions have long been used as indicators of the pressure and temperature of magmatic crystallization (Johnson & Rutherford, 1989; Schmidt, 1992). The application of this type of geothermometer or geobarometer has, however, been restricted to calc-alkaline systems. Recently, a method has been developed by which calcic amphibole compositions can be used as a thermobarometer for alkalic magma systems (Ridolfi & Renzulli, 2012). This method encompasses experimental data overlapping with the Ulleung whole-rock (phonolite) and mineral compositions (kaersutite) and can therefore be applied to our samples. Amphibole is present in the Ulleung phonolitic tephras of Stage 4 and in the Nari sequence porphyritic and phaneritic accidental lithics. Application of the Ridolfi & Renzulli (2012) thermobarometer to these samples (Fig. 13a) indicates that amphibole crystallized at pressures varying from *c.* 1600 MPa to *c.* 500 MPa. Amphibole in the porphyritic lithics mainly crystallized at *c.* 600 MPa. Amphibole in the phonolitic Tephras 1 and 2 similarly crystallized at *c.* 600 MPa; however, crystals in Tephra 5 yield crystallization pressures of 1200–1400 MPa. These higher-pressure amphiboles are also found in the phaneritic lithics (Fig. 13a).

To test the results obtained from amphibole thermobarometry, the generalized clinopyroxene thermobarometers of Putirka (2008) have also been applied, using his equation (32d) for temperature and equation (32a) for pressure and the Microsoft Excel® spreadsheet RiM69_Ch03_cpx_P-T.xls provided. The Putirka thermometers and barometers require the input of pressure and temperature respectively and are therefore not based solely on the clinopyroxene composition. For our models we selected an input temperature based on the liquidus temperature calculated with the software PELE (Boudreau, 1999), a constant pressure of 500 MPa (5 kbar) and added water content to the whole-rock compositions based on the amphibole hygrometer of Ridolfi & Renzulli (2012). The input parameters are summarized in Table 11. We selected constant pressure to provide a comparison on a similar basis and to avoid introducing further uncertainty (which would have affected the resulting model temperature), as input values can have a significant influence on the results. Increasing input T would result in lower P, and increasing input P would increase the estimate of T. As a proviso in interpreting these results it should be noted that the models have relatively large errors at ±310 MPa and ±58°C. Using these input parameters (Table 11) the calculated clinopyroxene temperatures and pressures are generally consistent with those obtained from the amphibole compositions as illustrated in Fig. 13b. The effusive trachytes tend to show

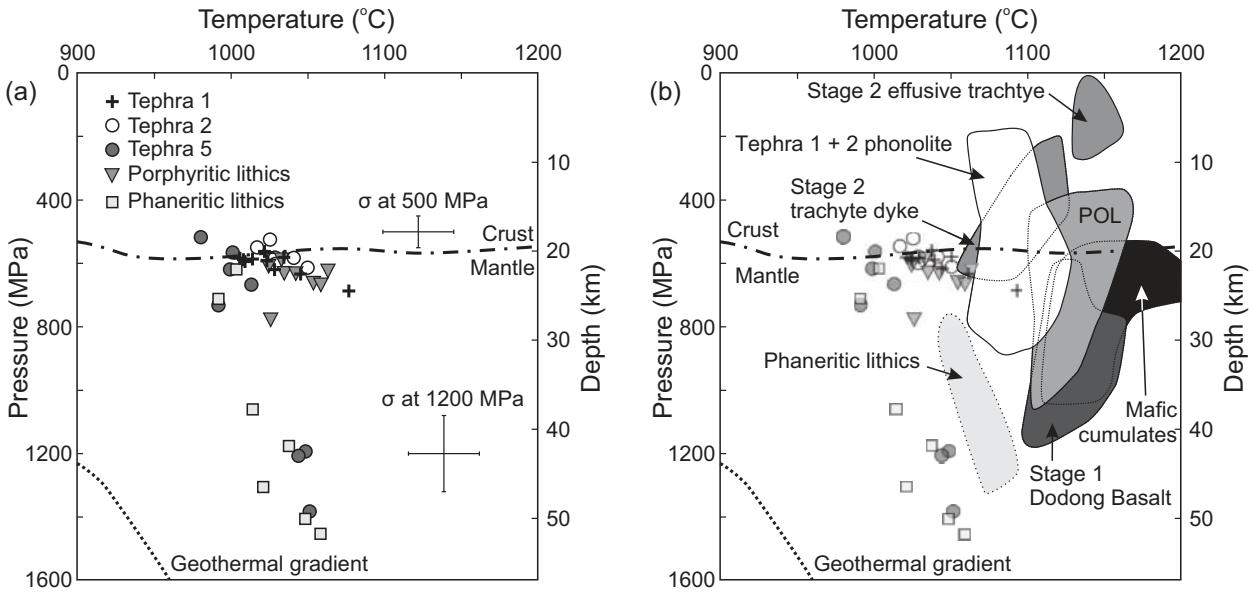

Fig. 13. Pressure and temperature estimates for crystallization of the Ulleung magmas. Models based on (a) amphibole compositions (Ridolfi & Renzulli, 2012) and (b) clinopyroxene (only) compositions (Putirka, 2008) with input parameters summarized in Table 11. POL is the field of porphyritic lithics. The geothermal gradient is from Choi *et al.* (2001). Crust–mantle boundary depth is from Kim *et al.* (2003).

Table 11: Input parameters for Putirka (2008) clinopyroxene thermobarometer based on thermodynamic calculations performed with the software PELE (Boudreau, 1999).

Sample	Stage	TAS composition	PELE model input parameters*		PELE results, liquidus	Input parameters for Putirka model	
			Added H_2O*	*P* (kbar)†	*T* (°C)‡	*T* (K)	*P* (kbar)†
UL12-5	4	tephriphonolite	4	5	1007	1227	5
UL12-9	4	phonolite	4	5	1117	1337	5
UL12-13	4	phonolite	4	5	958	1178	5
UL12-17	4	phonolite	4	5	1087	1307	5
UL09	2	trachyte	3	5	1076	1296	5
UL27	1	trachybasalt	1	5	1330	1550	5
UL28	2	trachyte	3	5	1108	1328	5
UL35	1	trachybasalt	1	5	1265	1485	5
NA05A	PO	tephriphonolite	3	5	1275	1495	5
NA05B	PO	trachyandesite	3	5	1053	1273	5
NA05E	4	phonolite	4	5	968	1188	5
NA11A	PH	tephriphonolite§	5	5	1050	1220	5
NA11E	CM	basalt§	1	5	1359	1529	5

*Water added to dry whole-rock compositions based on the amphibole thermobarometric results of Ridolfi & Renzulli (2012), and arbitrarily set as 1 wt % for mafic compositions.
†Input pressure arbitrarily set as 5 kbar (500 MPa) for all rock types to provide comparison on a similar basis (note that input pressure does not affect output pressure).
‡Liquidus temperature with computed NNO redox.
§Extrusive terminology but rocks are intrusive.

the highest crystallization temperatures (except for the mafic cumulates) and lower pressures, whereas the phaneritic lithics show the higher crystallization pressures. The overlap between Stage 1 Dodong Basalt and the mafic cumulate temperatures and pressures is noteworthy, again testifying to their consanguinity.

A further estimate of crystallization pressures was obtained using the software PELE (Boudreau, 1999), which is based on the MELTS thermodynamic models and numerical algorithms (Hirschmann & Ghiorso, 1994; Ghiorso & Sack, 1995). We used whole-rock compositions for selected Stage 2 trachyte and Stage 4 phonolite samples with added water contents consistent with those used above and summarized in Table 11. We subsequently ran the isobaric fractionation models with differing input pressures to estimate the pressure conditions under which chemical evolution of most major elements in the Ulleung suites is re-created (Supplementary Data Electronic Appendix 3). The model results indicate that variability within the Stage 2+3 trachytes is best reproduced at less than 500 MPa. Conversely, the SiO_2 depletion observed in the Stage 4 phonolite suite (from Tephra 2 to Tephra 5; Fig. 3b) requires pressures of 1000–1500 MPa. Below these pressures no model reproduces the observed chemical variation. The modelled fractionation assemblages are dominantly feldspars with minor pyroxene, olivine, apatite and oxides, consistent with our fractionation models above (Table 10).

Consideration of the P–T *modelling results*

The higher pressure amphiboles identified from application of the Ridolfi & Renzulli (2012) thermobarometer tend to have larger apparent errors and may therefore be unreliable (F. Ridolfi, personal communication, 2013). However, there is a correlation between the higher pressure amphiboles and pressures derived from clinopyroxene models (Putirka, 2008), and the simulations made using the software PELE lend additional support for deep fractionation of Stage 4 phonolites. Thus, we consider that the amphibole thermobarometry provides reliable estimates of the actual pressures and temperatures of crystallization. The nepheline temperature of crystallization was estimated to be >775°C (Hamilton, 1961; Fig. 6) and given that this is one of the last crystallizing phases (Fudali, 1963), trachytic to phonolitic magma temperatures in the plumbing system of the volcano were probably >800–900°C. By comparison, temperatures for phonolitic magma in excess of 1000°C have been measured at Mount Erebus, Antarctica (Burgisser *et al.*, 2012).

The absence of amphibole in the trachytic lavas of Stages 2 + 3 prevents a direct thermobarometric comparison with the phonolitic tephras of Stage 4. Nonetheless, results from the clinopyroxene thermobarometer appear consistent with the amphibole approach (Fig. 13). Additionally, the PELE simulations also suggest that the phonolitic and trachytic magmas evolved under different pressure conditions. Phonolites were derived from a relatively cooler magma that evolved at higher pressure (~600–1000 MPa). Such pressures correspond to the base of the crust (~20 km, 500–600 MPa) and upper lithospheric mantle (Kim *et al.*, 2003), and are consistent with experimentally determined lines of descent in alkali magmas at high pressures (Irving & Green, 2008). Moreover, Tephra 5 contains amphibole that crystallized at even higher pressure (1200 MPa). This amphibole has a thin rim that crystallized at low pressure (730 MPa; Fig. 14). This suggests that at least some phonolitic magmas ascended relatively rapidly from mantle depths shortly before eruption, and this may have facilitated the ascent of further phonolite magma to the lower crust. In contrast, Stage 2 + 3 trachytes evolved within the crust at pressures <500 MPa. Pressure estimates obtained from the phaneritic lithics are also higher than those for the Stage 2 + 3 trachytes. As noted above, based on their trace element and isotopic compositions, the phaneritic lithics are, however, more likely to be linked to the younger (Stage 4) magmatic system that fed the explosive phonolitic eruptions, which is consistent with the higher pressures estimated for the phaneritic lithics.

Coexisting ilmenite and magnetite have been analysed in samples NA05A (porphyritic accidental lithic, tephriphonolite) and UL27 (Stage 1, trachybasalt). Based on the approach of Spencer & Lindsley (1981) and the worksheet of Lepage (2003), sample NA05A gives temperatures of 684 and 692°C and $\log_{10} fO_2$ of −16·2 and −16·4, whereas sample UL27 gives a temperature of 1032°C and $\log_{10} fO_2$ of −9·6. The temperature estimated for the porphyritic accidental lithic sample is below the estimates obtained by the amphibole method and suggests that the exsolution of ilmenite from magnetite has taken place during subsolidus alteration. Oxygen fugacity is close to the nickel–nickel oxide (NNO) buffer and in agreement with the amphibole-based geothermobarometer–hygrometer of Ridolfi & Renzulli (2012). The latter model yields results varying from NNO to NNO + 2 for trachytes and phonolites and up to NNO + 3·6 for the phaneritic lithics. Water content based on this model tends to be 3–4 wt % for trachytes, 3·5–7 wt % for phonolites and 5–8 wt % for the phaneritic lithics.

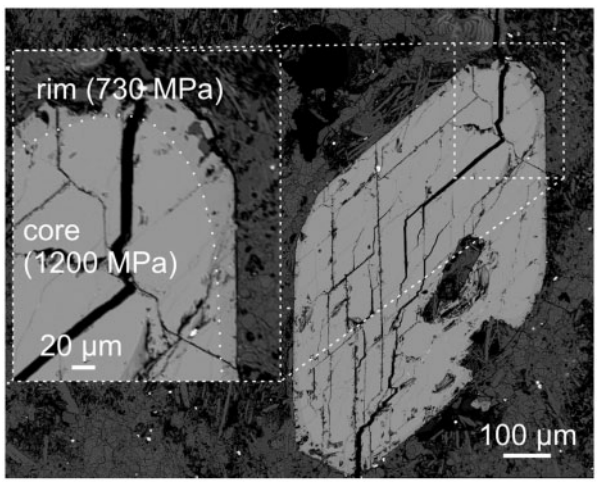

Fig. 14. Scanning electron microscope (SEM) image of an amphibole in sample UL12/18 (Tephra 5), which shows distinctly different crystallization pressures between core and rim, but does not show disequilibrium features.

Biotite is commonly present in the Stage 2 + 3 trachytic rocks, but is less common in the Stage 4 phonolite samples. The latter are the only ones that contain amphibole, including the associated porphyritic lithics. Rims of biotite around amphibole are indications that as the magma shifted to higher levels in the system, water contents rose in the residual melt and crystallization of biotite became preferred. This is consistent with thermobarometric evidence for a deeper storage site for the phonolite magmas compared with the trachytes. Freise *et al.* (2003) determined that biotite crystallization is suppressed under more oxidizing conditions (NNO + 2·3), which would have been the case for the phaneritic rocks. By comparison, greater oxidizing conditions at depth have been envisaged for the magmatic system of Erebus (Moussallam *et al.*, 2013). Given that both Ulleung trachytes and phonolites crystallized at NNO + 0 to + 2, it is unlikely that the oxidation state alone is a cause of the different proportions of biotite in the two magma types.

Based on his work on the leucite-bearing rocks erupted in the post-caldera stage at Ulleung (our Tephra 1, Stage 4), Tsuboi (1981) suggested that this latest known magma to be erupted at Ulleung was derived from pressures >260 MPa and temperatures in excess of 950°C. These values are based on experiments carried out with 6% H_2O (Goranson, 1938), whereas the amphibole hygrometry (Ridolfi & Renzulli, 2012) indicates that the magma H_2O content was *c.* 4%. Thus the actual temperature and pressure are likely to be considerably higher, consistent with the amphibole thermobarometry (Fig. 13).

These temperature and pressure constraints could shed some light on the debate about the origin of the Daly Gap in alkalic magma systems. The relatively primitive compositions of Stage 1 are distinct from the later trachytes of Stages 2 + 3 and the phonolites of Stage 4. Although the Stage 1 and Stage 2 lavas could be linked via crystal fractionation processes, this occurred at different depths

within the magmatic system (Fig. 13b). Nevertheless, some trachytic dykes belonging to Stage 2 and the porphyritic lithics have relatively more primitive compositions (trachyandesite or tephriphonolite; Fig. 3). This is consistent with separation of upward migrating magmas followed by subsequent storage and further fractionation, as proposed by Dufek & Bachmann (2010).

Magmatic evolution controls on eruption style

At Ulleung trachytic magmas were mainly erupted effusively, whereas phonolites were erupted explosively from a caldera. Given the pressure and temperature determinations based on mineral chemistry and whole-rock compositions, we consider that the magma feeding the Stage 4 phonolitic tephras was derived from deep storage at greater pressure than the magmas of the earlier Stage 2 and 3 trachytic eruptions. The distinct isotopic characteristics and relatively constant $^{87}Sr/^{86}Sr$ with increasing Th abundance in the Stage 4 samples (Fig. 11e) suggest that a new magma batch arrived in the deep plumbing system of the volcano, evolved and erupted relatively rapidly over *c.* 20 kyr without significant time for crustal assimilation. This contrasts to the pre-eruption processes for the earlier Stage 2 trachytic magmatism. The trachytes have a greater isotopic variability, which prompted Kim *et al.* (1999) to propose that crustal assimilation and seawater alteration were involved in their petrogenesis. This, coupled with a generally lower fractionation pressure and a period of trachytic volcanism spanning *c.* 600 kyr, is an indication that the trachytic magmas spent more time in shallow reservoirs prior to eruption. Stage 3 is also trachytic; however, it shows transitional characteristics between Stages 2 and 4. Therefore, the process of deepening sites of magma storage in the plumbing system of Ulleung occurred stepwise and slowly.

Temperature and pressure conditions obtained for the Ulleung eruptive rocks can be compared with those for other phonolitic eruptions. These are generally estimated at <250 MPa and <850°C (Berndt *et al.*, 2001; Freise *et al.*, 2003; Scaillet *et al.*, 2008; Andújar & Scaillet, 2012), although systems at higher temperature and pressure are also known (Irving & Green, 2008; Kelly *et al.*, 2008; Burgisser *et al.*, 2012). Andújar & Scaillet (2012) observed that magmas stored at pressures greater than those required for water saturation are likely to erupt effusively, or show transient effusive–explosive behaviour. Based on the pressure and H_2O estimates obtained for Ulleung and estimates of H_2O solubility in trachytic and phonolitic magmas (Carroll & Blank, 1997; Di Matteo *et al.*, 2004) the Ulleung magmas were H_2O undersaturated, except possibly for those represented by the phaneritic lithics and Tephra 5 for which H_2O >7 wt %. The phaneritic lithic sample with interstitial micro-vesiculated glass was unlikely to have been completely solid at the time it was entrained in an erupting magma (the interstitial glass is likely to have been similar in composition to the phonolitic tephra). The fact that the glass vesiculated suggests that it represents residual melt containing dissolved volatiles (H_2O), rather than being the result of remelting of syenitic country rock. A sudden decompression owing to the opening of the system coupled with entrainment and ascent of the lithic material during eruption of the phonolite tephra would have caused H_2O saturation conditions and hence vesiculation in the interstitial magma. Our model is summarized in Fig. 15.

The mafic cumulates are included in the Stage 4 phonolite tephras and therefore they must have been entrained in the rising magma just prior to eruption. This suggests that the Stage 4 phonolites were residing at the same or a deeper level compared with the site of crystallization of the units represented by the xenoliths. This hypothesis is consistent with the thermobarometry results (Fig. 13b). The mineral phases in the phonolitic tephras are consistent with the suggestion that the magma from which the phonolitic tephra was derived was crystallizing at the same level as or deeper than the units represented by the mafic cumulates.

Consideration of the Stage 4 phonolite in relation to analogous magmatic systems

The explosive character of the phonolitic eruptions at Ulleung contrasts with the magmatic system at Mount Erebus, Antactica. There, phonolitic magma forms a lava lake connected to the deeper magmatic system, which allows continuous degassing (Oppenheimer *et al.*, 2011). Such an open 'mantle to surface' system (Oppenheimer *et al.*, 2011) prevents the build-up of volatiles and hence the occurrence of large explosive eruptions. In contrast to Ulleung, the magma composition at Erebus has remained constant over the past 17 kyr (Kelly *et al.*, 2008) following homogenization of the magmatic system post *c.* 250 ka (Sims *et al.*, 2008). Although at Ulleung the magmas feeding each large explosive eruption were distinct, they were nonetheless related to a common parental melt. Their independent eruption suggests that the Ulleung magmatic system consists of a system of vertically dispersed magma batches. The ascent of one batch does not establish a viable plumbing system for continuous magma ascent or convection and degassing activity.

At Mount Vesuvius relatively recent large explosive eruptions show a transition from initial phonolitic tephras to more 'mafic' phonotephritic compositions (Civetta *et al.*, 1991). This transition was interpreted by Civetta *et al.* (1991) as indicating magma mixing and recharge forming layering within a magma chamber. These magma reservoirs are likely to be at a variety of depths (<10–15 km) beneath the volcano (Marianelli *et al.*, 1999; Webster *et al.*, 2001). Similarly, the magmatic system at Teide–Pico Viejo on Tenerife, Canary Islands, has been interpreted to be

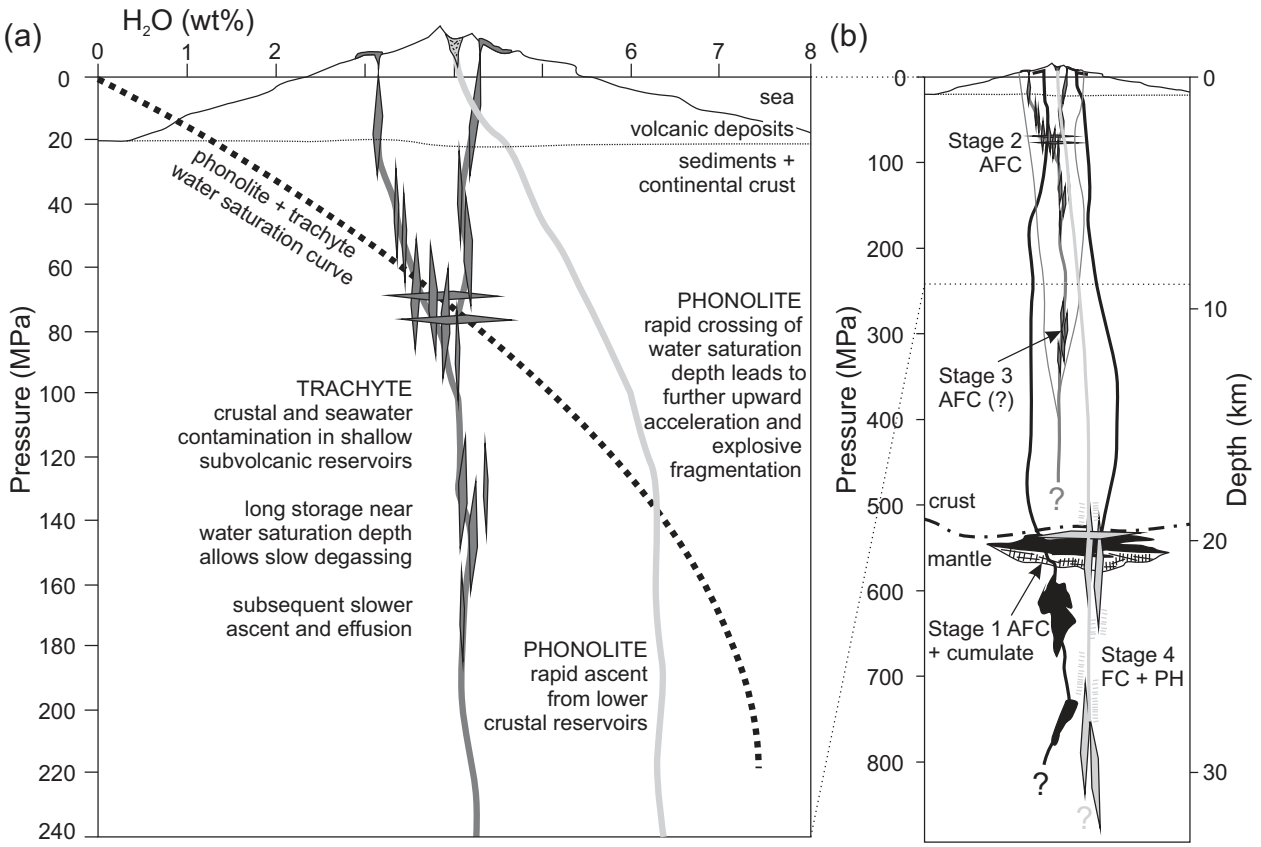

Fig. 15. (a) Schematic diagram illustrating the different modes of ascent of trachytic and phonolitic magmas at Ulleung volcano. The water saturation curve is from Di Matteo *et al.* (2004). (b) Schematic representation of the magmatic system of Ulleung volcano. Lower crustal assimilation and fractional crystallization (AFC) during Stage 1 basaltic magma evolution with accumulation and formation of mafic cumulates. Stages 2 and 3 evolution via AFC at shallower crustal levels, possibly becoming deeper during Stage 3. Stage 4 lower crustal–upper mantle fractional crystallization (FC) and formation of crystal mushes later entrained as phaneritic accidental lithics (PH).

composed of a series of shallow reservoirs connected with a recharging system at greater depth (Ablay *et al.*, 1998). At Ulleung, each large explosive eruption has an almost uniform composition, although over the past 20 kyr the composition shifted from the initially more extremely evolved Tephra 5 phonolite compositions to the final Tephra 1 tephriphonolite, with intermediate composition Tephras 2–4 between them. This sequence suggests some degree of interconnectedness between the different magma pockets in the deep plumbing system at Ulleung.

A distinct characteristic of the Ulleung magmatic system is that activity ceased after the last eruption (Tephra 1), whereas the other phonolitic volcanoes discussed above are sites of continuing activity, although not necessarily phonolitic. In this sense, Ulleung is more akin to the phonolitic eruption of Laacher See, Germany (Wörner & Schmincke, 1984), which occurred within a dispersed 'monogenetic' volcanic field. This characteristic of Ulleung points to a lack of an established Holocene magma plumbing system, which may be a result of the very deep (sub-crustal) source of the last episode of magmatism.

Other Quaternary intraplate volcanoes in east Asia (e.g. Jeju and Changbaishan) do not show lineages evolving to phonolite. Both Jeju and Changbaishan lie on thicker continental crust (~35–40 km; Hetland *et al.*, 2004; Yoo *et al.*, 2007). At Jeju, magmatic evolution occurred at both middle and lower crustal depths over relatively long amounts of time (several tens of thousands to hundreds of thousands of years; Brenna *et al.*, 2012). At Changbaishan the time between magma injection in the crust and the time of eruption was considerably shorter (<20 kyr; Zou *et al.*, 2010). These differences from and analogies with the Ulleung system suggest that crustal thickness in itself does not necessarily control the evolutionary lineage as much as a combination of the site and the timing and duration of magmatic evolution.

CONCLUSIONS

Ulleung Island is an alkalic intraplate volcano that evolved from a basaltic shield to a summit consisting of trachyte and phonolite eruptive rocks. Eruption of the latter was

associated with formation of a caldera. Samples have been analysed from the surface eruptive units, as well as accidental lithics brought to the surface by the explosive eruptions and representing various components of the evolving plumbing system of the volcano. Magmas were fed into the plumbing system of the volcano at episodic intervals, with initial basaltic activity evolving by fractional crystallization at lower crustal levels and leaving behind mafic cumulates. Chemically related magmas, which are not likely to be from the same line of descent, were injected later at shallower crustal levels and evolved to trachytes before eruption. The last phase of activity is associated with a chemically distinct magma derived from a different portion of a heterogeneous source. This last magma evolved to phonolitic compositions at lower crustal to upper mantle levels, leaving behind intrusive (phaneritic) residues, fragments of which were later also erupted as accidental lithics.

In addition to being fed by two distinct and compositionally different parental magmas, trachytic (Stage 2+3) and phonolitic (Stage 4) eruptive phases erupted effusively and explosively, respectively. This contrast was due to differences in the final magma storage conditions. The phonolitic magmas that erupted explosively were stored at deeper levels (subcrustal, 600–1000 MPa) and for a shorter periods (tens of thousands of years), without significantly assimilating crustal material. Conversely, the trachytic magmas evolved higher in the crust (<500 MPa) for longer time intervals and consequently they were contaminated by their crustal surroundings, degassed and erupted effusively. This may indicate that final magma ascent from a depth greater than that of water saturation favors explosivity during eruption, whereas storage for longer periods at a shallower depth leads to thorough degassing and effusive trachytic eruptions.

Ulleung is a distinct case of an intraplate alkalic volcano. It has characteristics in common with better-known magmatic systems that evolved to phonolite (e.g. Erebus, Vesuvius); however, it shows remarkable differences. Importantly, it appears to have evolved into a volcanic system fed by deep magma reservoirs with activity subsiding following its latest brief distinct magmatic pulse. This type of reawakening activity may pose a greater hazard because it is much less predictable.

ACKNOWLEDGEMENTS

John Wilmshurst helped with XRF analytical work. Jong Ok Jeong assisted on the electron microprobe at Gyeongsang National University. Richard Wysoczanski and two anonymous reviewers provided thorough and insightful comments. Simon Turner is thanked for editorial handling.

FUNDING

This work is supported by the FRST-MSI project MAUX0808 'Facing the challenge of Auckland volcanism', by the New Zealand Natural Hazards Research Platform, and by a National Research Foundation of Korea (NRF) grant to Y.K.S. (No. 2009-0079427).

SUPPLEMENTARY DATA

Supplementary data for this paper are available at *Journal of Petrology* online.

REFERENCES

Ablay, G. J., Carroll, M. R., Palmer, M. R., Martí, J. & Sparks, R. S. J. (1998). Basanite–phonolite lineages of the Teide–Pico Viejo volcanic complex, Tenerife, Canary Islands. *Journal of Petrology* **39**, 905–936.

Allibon, J., Ovtcharova, M., Bussy, F., Cosca, M., Schaltegger, U., Bussien, D. *et al*. (2011). Lifetime of an ocean island volcano feeder zone: constraints from U–Pb dating on coexisting zircon and baddeleyite, and $^{40}Ar/^{39}Ar$ age determinations, Fuerteventura, Canary Islands. *Canadian Journal of Earth Sciences* **48**, 567–592.

Andújar, J. & Scaillet, B. (2012). Experimental constraints on parameters controlling the difference in the eruptive dynamics of phonolitic magmas: the case of Tenerife (Canary Islands). *Journal of Petrology* **53**, 1777–1806.

Andújar, J., Costa, F., Martí, J., Wolff, J. A. & Carroll, M. R. (2008). Experimental constraints on pre-eruptive conditions of phonolitic magma from the caldera-forming El Abrigo eruption, Tenerife (Canary Islands). *Chemical Geology* **257**, 173–191.

Bailey, D. K. (1964). Crustal warping, a possible tectonic control of alkaline magmatism. *Journal of Geophysical Research* **69**, 1103–1111.

Bailey, S. W. (1984). Classification and structures of the micas. In: Bailey, S. W. (ed.) *Micas. Mineralogical Society of America, Reviews in Mineralogy* **13**, 1–12.

Baker, I. (1969). Petrology of the volcanic rocks of Saint Helena Island, South Atlantic. *Geological Society of America Bulletin* **80**, 1283–1310.

Barling, J., Goldstein, S. L. & Nicholls, I. A. (1994). Geochemistry of Heard Island (southern Indian Ocean): characterization of an enriched mantle component and implications for enrichment of the sub-Indian Ocean mantle. *Journal of Petrology* **35**, 1017–1053.

Berndt, J., Holtz, F. & Koepke, J. (2001). Experimental constraints on storage conditions in the chemically zoned phonolitic magma chamber of the Laacher See volcano. *Contributions to Mineralogy and Petrology* **140**, 469–486.

Blundy, J. & Wood, B. (2003). Mineral–melt partitioning of uranium, thorium and their daughters. In: Bourdon, B., Henderson, G. M., Lundstrom, C. C. & Turner, S. P. (eds) *U-series Geochemistry. Mineralogical Society of America and Geochemical Society, Reviews in Mineralogy and Geochemistry* **52**, 59–123.

Boudreau, A. E. (1999). PELE—a version of the MELTS software program for the PC platform. *Computers and Geosciences* **25**, 201–203.

Brenna, M., Cronin, S. J., Smith, I. E. M., Sohn, Y. K. & Maas, R. (2012). Spatio-temporal evolution of a dispersed magmatic system and its implications for volcano growth, Jeju Island Volcanic Field, Korea. *Lithos* **148**, 337–352.

Burgisser, A., Oppenheimer, C., Alletti, M., Kyle, P. R., Scaillet, B. & Carroll, M. R. (2012). Backward tracking of gas chemistry measurements at Erebus volcano. *Geochemistry, Geophysics, Geosystems* **13**, Q11010, doi: 10.1029/2012GC004243.

Carroll, M. R. & Blank, J. G. (1997). The solubility of H_2O in phonolitic melts. *American Mineralogist* **82**, 549–556.

Castro, J. M. & Gardner, J. E. (2008). Did magma ascent rate control the explosive–effusive transition at the Inyo volcanic chain, California? *Geology* **36**, 279–282.

Cheong, C.-S., Kwon, S.-T. & Sagong, H. (2002). Geochemical and Sr–Nd–Pb isotopic investigation of Triassic granitoids and basement rocks in the northern Gyeongsang Basin, Korea: implications for the young basement in the East Asian continental margin. *Island Arc* **11**, 25–44.

Choi, S. H., Jwa, Y. J. & Lee, H. Y. (2001). Geothermal gradient of the upper mantle beneath Jeju Island, Korea: evidence from mantle xenoliths. *Island Arc* **10**, 175–193.

Choi, S. H., Kwon, S. T., Mukasa, S. B. & Sagong, H. (2005). Sr–Nd–Pb isotope and trace element systematics of mantle xenoliths from Late Cenozoic alkaline lavas, South Korea. *Chemical Geology* **221**, 40–64.

Choi, S. H., Mukasa, S. B., Kwon, S. T. & Andronikov, A. V. (2006). Sr, Nd, Pb and Hf isotopic compositions of late Cenozoic alkali basalts in South Korea: evidence for mixing between the two dominant asthenospheric mantle domains beneath East Asia. *Chemical Geology* **232**, 134–151.

Civetta, L., Galati, R. & Santacroce, R. (1991). Magma mixing and convective compositional layering within the Vesuvius magma chamber. *Bulletin of Volcanology* **53**, 287–300.

Coombs, D. S. & Wilkinson, J. F. G. (1969). Lineages and fractionation trends in undersaturated volcanic rocks from the East Otago Volcanic Province (New Zealand) and related rocks. *Journal of Petrology* **10**, 440–501.

De Fino, M., Volpe, L., Peccerillo, A., Piccarreta, G. & Poli, G. (1986). Petrogenesis of Monte Vulture volcano (Italy): inferences from mineral chemistry, major and trace element data. *Contributions to Mineralogy and Petrology* **92**, 135–145.

Di Matteo, V., Carroll, M. R., Behrens, H., Vetere, F. & Brooker, R. A. (2004). Water solubility in trachytic melts. *Chemical Geology* **213**, 187–196.

Dufek, J. & Bachmann, O. (2010). Quantum magmatism: magmatic compositional gaps generated by melt–crystal dynamics. *Geology* **38**, 687–690.

Dunn, T. & Sen, C. (1994). Mineral/matrix partition coefficients for orthopyroxene, plagioclase, and olivine in basaltic to andesitic systems: a combined analytical and experimental study. *Geochimica et Cosmochimica Acta* **58**, 717–733.

Dupré, B. & Allègre, C. J. (1983). Pb–Sr isotope variation in Indian Ocean basalts and mixing phenomena. *Nature* **303**, 142–146.

Edwards, B., Russell, J. & Anderson, R. (2002). Subglacial, phonolitic volcanism at Hoodoo Mountain volcano, northern Canadian Cordillera. *Bulletin of Volcanology* **64**, 254–272.

Eggins, S. M., Rudnick, R. L. & McDonough, W. F. (1998). The composition of peridotites and their minerals: a laser-ablation ICP–MS study. *Earth and Planetary Science Letters* **154**, 53–71.

Elburg, M. A., Vroon, P., van der Wagt, B. & Tchalikian, A. (2005). Sr and Pb isotopic composition of five USGS glasses (BHVO-2G, BIR-1G, TB-1G, NKT-1G). *Chemical Geology* **223**, 196–207.

Ewart, A. & Hawkesworth, C. J. (1987). The Pleistocene–Recent Tonga–Kermadec arc lavas: interpretation of new isotopic and rare earth data in terms of a depleted mantle source model. *Journal of Petrology* **28**, 495–530.

Ferla, P. & Meli, C. (2006). Evidence of magma mixing in the 'Daly Gap' of alkaline suites: a case study from the enclaves of Pantelleria (Italy). *Journal of Petrology* **47**, 1467–1507.

Francis, D. & Ludden, J. (1995). The signature of amphibole in mafic alkaline lavas, a study in the northern Canadian Cordillera. *Journal of Petrology* **36**, 1171–1191.

Freise, M., Holtz, F., Koepke, J., Scoates, J. & Leyrit, H. (2003). Experimental constraints on the storage conditions of phonolites from the Kerguelen Archipelago. *Contributions to Mineralogy and Petrology* **145**, 659–672.

Fudali, R. F. (1963). Experimental studies bearing on the origin of pseudoleucite and associated problems of alkalic rock systems. *Geological Society of America Bulletin* **74**, 1101–1126.

Ghiorso, M. & Sack, R. (1995). Chemical mass transfer in magmatic processes IV. A revised and internally consistent thermodynamic model for the interpolation and extrapolation of liquid–solid equilibria in magmatic systems at elevated temperatures and pressures. *Contributions to Mineralogy and Petrology* **119**, 197–212.

Goranson, R. W. (1938). Silicate–water system: phase equilibria in the $NaAlSi_3O_8$–H_2O and $KAlSi_3O_8$–H_2O systems at high temperatures and pressures. *American Journal of Science* **35**, 72–91.

Halliday, A. N., Lee, D.-C., Tommasini, S., Davies, G. R., Paslick, C. R., Fitton, G. J. *et al.* (1995). Incompatible trace elements in OIB and MORB and source enrichment in the sub-oceanic mantle. *Earth and Planetary Science Letters* **133**, 379–395.

Hamilton, D. L. (1961). Nephelines as crystallization temperature indicators. *Journal of Geology* **69**, 321–329.

Hart, S. R. (1984). A large-scale isotope anomaly in the Southern Hemisphere mantle. *Nature* **309**, 753–757.

Hart, S. R., Hauri, E. H., Oschmann, L. A. & Whitehead, J. A. (1992). Mantle plumes and entrainment: isotopic evidence. *Science* **256**, 517–520.

Hay, D. E. & Wendlandt, R. F. (1995). The origin of Kenya rift plateau-type flood phonolites: results of high-pressure/high-temperature experiments in the systems phonolite–H_2O and phonolite–H_2O–CO_2. *Journal of Geophysical Research: Solid Earth* **100**, 401–410.

Hay, D. E., Wendlandt, R. F. & Wendlandt, E. D. (1995). The origin of Kenya rift plateau-type flood phonolites: evidence from geochemical studies for fusion of lower crust modified by alkali basaltic magmatism. *Journal of Geophysical Research: Solid Earth* **100**, 411–422.

Hémond, C., Devey, C. W. & Chauvel, C. (1994). Source compositions and melting processes in the Society and Austral plumes (South Pacific Ocean): element and isotope (Sr, Nd, Pb, Th) geochemistry. *Chemical Geology* **115**, 7–45.

Hetland, E. A., Wu, F. T. & Song, J. L. (2004). Crustal structure in the Changbaishan volcanic area, China, determined by modeling receiver functions. *Tectonophysics* **386**, 157–175.

Hirschmann, M. M. & Ghiorso, M. S. (1994). Activities of nickel, cobalt, and manganese silicates in magmatic liquids and applications to olivine/liquid and to silicate/metal partitioning. *Geochimica et Cosmochimica Acta* **58**, 4109–4126.

Hobson, A., Bussy, F. & Hernandez, J. (1998). Shallow-level migmatization of gabbros in a metamorphic contact aureole, Fuerteventura Basal Complex, Canary Islands. *Journal of Petrology* **39**, 1025–1037.

Icenhower, J. & London, D. (1996). Experimental partitioning of Rb, Cs, Sr, and Ba between alkali feldspar and peraluminous melt. *American Mineralogist* **81**, 719–734.

Im, J., Shim, S., Choo, C., Jang, Y. & Lee, J. (2012). Volcanological and paleoenvironmental implications of charcoals of the Nari Formation in Nari Caldera, Ulleung Island, Korea. *Geosciences Journal* **16**, 105–114.

Irving, A. J. & Green, D. H. (2008). Phase relationships of hydrous alkalic magmas at high pressures: production of nepheline hawaiitic to mugearitic liquids by amphibole-dominated fractional

crystallization within the lithospheric mantle. *Journal of Petrology* **49**, 741–756.

Johansen, T. S., Hauff, F., Hoernle, K., Klügel, A. & Kokfelt, T. F. (2005). Basanite to phonolite differentiation within 1550–1750 yr: U–Th–Ra isotopic evidence from the A.D. 1585 eruption on La Palma, Canary Islands. *Geology* **33**, 897–900.

Johnson, M. C. & Rutherford, M. J. (1989). Experimental calibration of the aluminum-in-hornblende geobarometer with application to Long Valley caldera (California) volcanic rocks. *Geology* **17**, 837–841.

Kelly, P. J., Kyle, P. R., Dunbar, N. W. & Sims, K. W. W. (2008). Geochemistry and mineralogy of the phonolite lava lake, Erebus volcano, Antarctica: 1972–2004 and comparison with older lavas. *Journal of Volcanology and Geothermal Research* **177**, 589–605.

Kim, G. B., Yoon, S. H., Chough, S. K., Kwon, Y. K. & Ryu, B. J. (2011). Seismic reflection study of acoustic basement in the South Korea Plateau, the Ulleung Interplain Gap, and the northern Ulleung Basin: volcano-tectonic implications for Tertiary back-arc evolution in the southern East Sea. *Tectonophysics* **504**, 43–56.

Kim, H.-J., Jou, H.-T., Cho, H.-M., Bijwaard, H., Sato, T., Hong, J.-K. *et al.* (2003). Crustal structure of the continental margin of Korea in the East Sea (Japan Sea) from deep seismic sounding data: evidence for rifting affected by the hotter than normal mantle. *Tectonophysics* **364**, 25–42.

Kim, K. H., Tanaka, T., Nagao, K. & Jang, S. K. (1999). Nd and Sr isotopes and K–Ar ages of the Ulreungdo alkali volcanic rocks in the East Sea, South Korea. *Geochemical Journal* **33**, 317–341.

Kim, K. H., Nagao, K., Sumino, H., Tanaka, T., Hayashi, T., Nakamura, T. *et al.* (2008). He–Ar and Nd–Sr isotopic compositions of late Pleistocene felsic plutonic back arc basin rocks from Ulleungdo volcanic island, South Korea: implications for the genesis of young plutonic rocks in a back arc basin. *Chemical Geology* **253**, 180–195.

Kim, Y. K. (1985). Petrology of Ulreung volcanic island, Korea—Part 1. Geology. *Journal of the Japanese Association of Mineralogists, Petrologists and Economic Geologists* **80**, 128–135.

Kim, Y. K. (1986). Magmatic differentiation in the volcanic rocks from Ulreung Island, Korea. *Journal of the Japanese Association of Mineralogists, Petrologists and Economic Geologists* **81**, 165–180.

Kim, Y. K. & Fujimaki, H. (1987). Plutonic inclusions and olivine in high-K volcanics from Ulreung Island, Korea. *Mineralogy and Petrology* **37**, 117–136.

Klein, M., Stosch, H. G. & Seck, H. A. (1997). Partitioning of high field-strength and rare-earth elements between amphibole and quartz-dioritic to tonalitic melts: an experimental study. *Chemical Geology* **138**, 257–271.

Leake, B. E., Woolley, A. R., Arps, C. E. S., Birch, W. D., Gilbert, M. C., Grice, J. D. *et al.* (1997). Nomenclature of amphiboles; report of the Subcommittee on Amphiboles of the International Mineralogical Association Commission on new minerals and mineral names. *Mineralogical Magazine* **61**, 295–321.

Le Bas, M. J., Lemaitre, R. W., Streckeisen, A. & Zanettin, B. (1986). A chemical classification of volcanic rocks based on the total alkali–silica diagram. *Journal of Petrology* **27**, 745–750.

Legendre, C., Maury, R. C., Caroff, M., Guillou, H., Cotten, J., Chauvel, C. *et al.* (2005). Origin of exceptionally abundant phonolites on Ua Pou Island (Marquesas, French Polynesia): partial melting of basanites followed by crustal contamination. *Journal of Petrology* **46**, 1925–1962.

LeMasurier, W. E., Futa, K., Hole, M. & Kawachi, Y. (2003). Polybaric evolution of phonolite, trachyte, and rhyolite volcanoes in eastern Marie Byrd Land, Antarctica: controls on peralkalinity and silica saturation. *International Geology Review* **45**, 1055–1099.

LeMasurier, W., Choi, S., Kawachi, Y., Mukasa, S. & Rogers, N. W. (2011). Evolution of pantellerite–trachyte–phonolite volcanoes by fractional crystallization of basanite magma in a continental rift setting, Marie Byrd Land, Antarctica. *Contributions to Mineralogy and Petrology* **162**, 1175–1199.

Lepage, K. D. (2003). ILMAT: an Excel worksheet for ilmenite–magnetite geothermometry and geobarometry. *Computers and Geosciences* **29**, 673–678.

Le Roex, A. P., Cliff, R. A. & Adair, B. J. I. (1990). Tristan da Cunha, South Atlantic: geochemistry and petrogenesis of a basanite–phonolite lava series. *Journal of Petrology* **31**, 779–812.

Maas, R., Kamenetsky, M. B., Sobolev, A. V., Kamenetsky, V. S. & Sobolev, N. V. (2005). Sr–Nd–Pb isotopic evidence for a mantle origin of alkali chlorides and carbonates in the Udachnaya kimberlite, Siberia. *Geology* **35**, 549–552.

Machida, H. & Arai, F. (1983). Extensive ash falls in and around the sea of Japan from large Late Quaternary eruptions. *Journal of Volcanology and Geothermal Research* **18**, 151–164.

Marianelli, P., Métrich, N. & Sbrana, A. (1999). Shallow and deep reservoirs involved in magma supply of the 1944 eruption of Vesuvius. *Bulletin of Volcanology* **61**, 48–63.

Martin, A., Cooper, A. & Dunlap, W. J. (2010). Geochronology of Mount Morning, Antarctica: two-phase evolution of a long-lived trachyte–basanite–phonolite eruptive center. *Bulletin of Volcanology* **72**, 357–371.

McDonough, W. F. & Sun, S. S. (1995). The composition of the Earth. *Chemical Geology* **120**, 223–253.

Morimoto, N., Fabries, J., Ferguson, A. K., Ginzburg, I. V., Ross, M., Seifert, F. A. *et al.* (1988). Nomenclature of pyroxenes. *American Mineralogist* **73**, 1123–1133.

Moussallam, Y., Oppenheimer, C., Scaillet, B. & Kyle, P. R. (2013). Experimental phase-equilibrium constraints on the phonolite magmatic system of Erebus Volcano, Antarctica. *Journal of Petrology* **54**, 1285–1307.

Nash, W. P. & Crecraft, H. R. (1985). Partition coefficients for trace elements in silicic magmas. *Geochimica et Cosmochimica Acta* **49**, 2309–2322.

Nash, W. P., Carmichael, I. S. E. & Johnson, R. W. (1969). The mineralogy and petrology of Mount Suswa, Kenya. *Journal of Petrology* **10**, 409–439.

Nielsen, R. L., Forsythe, L. M., Gallahan, W. E. & Fisk, M. R. (1994). Major- and trace-element magnetite–melt equilibria. *Chemical Geology* **117**, 167–191.

Norrish, K. & Hutton, J. T. (1969). An accurate X-ray spectrographic method for the analysis of a wide range of geological samples. *Geochimica et Cosmochimica Acta* **33**, 431–453.

Oppenheimer, C., Moretti, R., Kyle, P. R., Eschenbacher, A., Lowenstern, J. B., Hervig, R. L. *et al.* (2011). Mantle to surface degassing of alkalic magmas at Erebus volcano, Antarctica. *Earth and Planetary Science Letters* **306**, 261–271.

Panter, K. S., Kyle, P. R. & Smellie, J. L. (1997). Petrogenesis of a phonolite–trachyte succession at Mount Sidley, Marie Byrd Land, Antarctica. *Journal of Petrology* **38**, 1225–1253.

Park, M. H., Kim, I. S. & Shin, J. B. (2003). Characteristics of the late Quaternary tephra layers in the East/Japan Sea and their new occurrences in western Ulleung Basin sediments. *Marine Geology* **202**, 135–142.

Price, R. C. & Chappell, B. W. (1975). Fractional crystallisation and the petrology of Dunedin volcano. *Contributions to Mineralogy and Petrology* **53**, 157–182.

Price, R. C. & Taylor, S. R. (1973). The geochemistry of the Dunedin Volcano, East Otago, New Zealand: rare earth elements. *Contributions to Mineralogy and Petrology* **40**, 195–205.

Price, R. C., Cooper, A. F., Woodhead, J. D. & Cartwright, I. (2003). Phonolitic diatremes within the Dunedin Volcano, South Island, New Zealand. *Journal of Petrology* **44**, 2053–2080.

Price, R. C., Johnson, R. W., Gray, C. M. & Frey, F. A. (1985). Geochemistry of phonolites and trachytes from the summit region of Mt. Kenya. *Contributions to Mineralogy and Petrology* **89**, 394–409.

Prowatke, S. & Klemme, S. (2006). Trace element partitioning between apatite and silicate melts. *Geochimica et Cosmochimica Acta* **70**, 4513–4527.

Putirka, K. D. (2008). Thermometers and barometers for volcanic systems. In: Putirka, K. D. & Tepley, F. J., III (eds) *Minerals, Inclusions and Volcanic Processes. Mineralogical Society of America and Geochemical Society, Reviews in Mineralogy and Geochemistry* **69**, 61–120.

Raczek, I., Jochum, K. P. & Hofmann, A. W. (2003). Neodymium and strontium isotope data for USGS reference materials BCR-1, BCR-2, BHVO-1, BHVO-2, AGV-1, AGV-2, GSP-1, GSP-2 and eight MPI-DING reference glasses. *Geostandards Newsletter* **27**, 173–179.

Ridolfi, F. & Renzulli, A. (2012). Calcic amphiboles in calc-alkaline and alkaline magmas: thermobarometric and chemometric empirical equations valid up to 1,130°C and 2·2 GPa. *Contributions to Mineralogy and Petrology* **163**, 877–895.

Sano, Y., Terada, K. & Fukuoka, T. (2002). High mass resolution ion microprobe analysis of rare earth elements in silicate glass, apatite and zircon: lack of matrix dependency. *Chemical Geology* **184**, 217–230.

Sato, H. (1977). Nickel content of basaltic magmas: identification of primary magmas and a measure of the degree of olivine fractionation. *Lithos* **10**, 113–120.

Scaillet, B., Pichavant, M. & Cioni, R. (2008). Upward migration of Vesuvius magma chamber over the past 20,000 years. *Nature* **455**, 216–219.

Schmidt, M. (1992). Amphibole composition in tonalite as a function of pressure: an experimental calibration of the Al-in-hornblende barometer. *Contributions to Mineralogy and Petrology* **110**, 304–310.

Signorelli, S., Vaggelli, G. & Romano, C. (1999). Pre-eruptive volatile (H_2O, F, Cl and S) contents of phonolitic magmas feeding the 3550-year old Avellino eruption from Vesuvius, southern Italy. *Journal of Volcanology and Geothermal Research* **93**, 237–256.

Sims, K. W. W., Blichert-Toft, J., Kyle, P. R., Pichat, S., Gauthier, P.-J., Blusztajn, J. *et al.* (2008). A Sr, Nd, Hf, and Pb isotope perspective on the genesis and long-term evolution of alkaline magmas from Erebus volcano, Antarctica. *Journal of Volcanology and Geothermal Research* **177**, 606–618.

Spencer, K. L. & Lindsley, D. H. (1981). A solution model for coexisting iron–titanium oxides. *American Mineralogist* **66**, 619–652.

Stormer, J. C. J. & Nicholls, J. (1978). XLFRAC: a program for the interactive testing of magmatic differentiation models. *Computers and Geosciences* **4**, 143–159.

Sun, S. S. & McDonough, W. F. (1989). Chemical and isotopic systematics of oceanic basalts: implications for mantle composition and processes. In: Saunders, A. D. & Norry, M. J. (eds) *Magmatism in the Ocean Basins. Geological Society, London, Special Publications* **42**, 313–345.

Tamaki, K., Suyehiro, K., Allan, J., Ingle, J. C. & Pisciotto, K. A. (1992). Tectonic synthesis and implications of Japan Sea ODP Drilling. In: Tamaki, K. & Suyehiro, K. *et al.* (eds) *Proceedings of the Ocean Drilling Program, Scientific Results 127/128 Part 2.* Ocean Drilling Program, pp. 1333–1348.

Tanaka, T., Togashi, S., Kamioka, H., Amakawa, H., Kagami, H., Hamamoto, T. *et al.* (2000). JNdi-1: a neodymium isotopic reference in consistency with LaJolla neodymium. *Chemical Geology* **168**, 279–281.

Tiepolo, M., Oberti, R. & Vannucci, R. (2002). Trace-element incorporation in titanite: constraints from experimentally determined solid/liquid partition coefficients. *Chemical Geology* **191**, 105–119.

Tsuboi, S. (1920). On a leucite rock, vulsinitic vicoite, from Utsuryoto Island in the Sea of Japan. *Journal of the Geological Society of Japan* **27**, 91–104.

Tsuboi, S. (1981). On the genesis of leucite rock of Island Utsuryoto (Ullungdo, Korea). *Proceedings of the Japan Academy, Series B* **57**, 233–238.

Vance, D. & Thirlwall, M. F. (2002). An assessment of mass discrimination in MC-ICPMS using Nd isotopes. *Chemical Geology* **185**, 227–240.

Vidal, P., Chauvel, C. & Brousse, R. (1984). Large mantle heterogeneity beneath French Polynesia. *Nature* **307**, 536–538.

Webster, J. D., Raia, F., De Vivo, B. & Rolandi, G. (2001). The behavior of chlorine and sulfur during differentiation of the Mt. Somma–Vesuvius magmatic system. *Mineralogy and Petrology* **73**, 177–200.

Wei, H., Wang, Y., Jin, J., Gao, L., Yun, S. H. & Jin, B. (2007). Timescale and evolution of the intracontinental Tianchi volcanic shield and ignimbrite-forming eruption, Changbaishan, Northeast China. *Lithos* **96**, 315–324.

Weis, D., Frey, F. A., Leyrit, H. & Gautier, I. (1993). Kerguelen Archipelago revisited: geochemical and isotopic study of the Southeast Province lavas. *Earth and Planetary Science Letters* **118**, 101–119.

Weis, D., Kieffer, B., Maerschalk, C., Barling, J., de Jong, J., Williams, G. A. *et al.* (2006). High-precision isotopic characterization of USGS reference materials by TIMS and MC-ICP-MS. *Geochemistry, Geophysics, Geosystems* **7**, Q08006, doi:10.1029/2006GC001283.

White, J. C. (2003). Trace-element partitioning between alkali feldspar and peralkalic quartz trachyte to rhyolite magma. Part II: empirical equations for calculating trace-element partition coefficients of large-ion lithophile, high field-strength, and rare-earth elements. *American Mineralogist* **88**, 330–337.

White, J. C., Espejel-García, V. V., Anthony, E. Y. & Omenda, P. (2012). Open system evolution of peralkaline trachyte and phonolite from the Suswa volcano, Kenya rift. *Lithos* **152**, 84–104.

Wiesmaier, S., Troll, V. R., Carracedo, J. C., Ellam, R. M., Bindeman, I. & Wolff, J. A. (2012). Bimodality of lavas in the Teide–Pico Viejo succession in Tenerife—the role of crustal melting in the origin of recent phonolites. *Journal of Petrology* **53**, 2465–2495.

Williams, I. S., Cho, D.-L. & Kim, S. W. (2009). Geochronology, and geochemical and Nd–Sr isotopic characteristics, of Triassic plutonic rocks in the Gyeonggi Massif, South Korea: constraints on Triassic post-collisional magmatism. *Lithos* **107**, 239–256.

Wilson, M., Downes, H. & Cebriá, J.-M. (1995). Contrasting fractionation trends in coexisting continental alkaline magma series; Cantal, Massif Central, France. *Journal of Petrology* **36**, 1729–1753.

Woodhead, J. D. (2002). A simple method for obtaining highly accurate Pb isotope data by MC-ICP-MS. *Journal of Analytical Atomic Spectroscopy* **17**, 1–6.

Woodhead, J. D. & Devey, C. W. (1993). Geochemistry of the Pitcairn seamounts, I: source character and temporal trends. *Earth and Planetary Science Letters* **116**, 81–99.

Workman, R. K., Hart, S. R., Jackson, M., Regelous, M., Farley, K. A., Blusztajn, J. *et al.* (2004). Recycled metasomatized lithosphere as the origin of the Enriched Mantle II (EM2) end-member: evidence from

the Samoan Volcanic Chain. *Geochemistry, Geophysics, Geosystems* **5**, Q04008, doi: 10.1029/2003GC000623.

Wörner, G. & Schmincke, H.-U. (1984). Petrogenesis of the zoned Laacher See tephra. *Journal of Petrology* **25**, 836–851.

Wörner, G., Beusen, J. M., Duchateau, N., Gijbels, R. & Schmincke, H. U. (1983). Trace element abundances and mineral/melt distribution coefficients in phonolites from the Laacher See volcano (Germany). *Contributions to Mineralogy and Petrology* **84**, 152–173.

Yoo, H. J., Herrmann, R. B., Cho, K. H. & Lee, K. (2007). Imaging the three-dimensional crust of the Korean Peninsula by joint inversion of surface-wave dispersion and teleseismic receiver functions. *Bulletin of the Seismological Society of America* **97**, 1002–1011.

Zou, H., Fan, Q. & Zhang, H. (2010). Rapid development of the great Millennium eruption of Changbaishan (Tianchi) Volcano, China/North Korea: evidence from U–Th zircon dating. *Lithos* **119**, 289–296.